MASTER

Kinetic Investigation of K2CO3 Composite at Reactor-Scale to analyze its Charging & Discharging Performance

Awais, Muhammad

Award date:
2018

Technische Universiteit Eindhoven University of Technology

Department of Mechanical Engineering
Energy Technology Research Group

MSc SELECT – Environomical Pathways for Sustainable Energy Systems

Kinetic Investigation of K_2CO_3 Composite at Reactor-Scale to analyze its Charging & Discharging Performance

Master Thesis

Muhammad Awais
1279866
Sustainable Energy Technology
Mechanical Engineering
Eindhoven University of Technology

Thesis Supervisor:
Dr. ir. C.C.M. (Camilo) Rindt

Graduation Committee:
Prof. Dr. H.A. (Herbert) Zondag
Dr. ir. HP (Henk) Huinink

Coach:
Ir. Luca Scapino

Eindhoven, August 2018

Technische Universiteit
Eindhoven
University of Technology

Declaration concerning the TU/e Code of Scientific Conduct for the Master's Thesis

I have read the TU/e Code of Scientific Conduct[1].

I hereby declare that my master's thesis has been carried out in accordance with the rules of the TU/e Code of Scientific Conduct.

Date
22-08-2018

Name
Muhammad Awais

ID-number
1279866

Signature 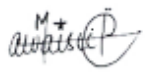

Submit the signed declaration to the student administration of your department.

[1]See: https://www.tue.nl/en/university/about-the-university/integrity/scientific-integrity/
The Netherlands Code of Conduct for Academic Practice of the VSNU can be found here also.
More information about scientific integrity is published on the websites of TU/e and VSNU

Dedicated to my parents

Acknowledgments

At the end of the graduation project, I would like to express my special thanks to all the people who were involved directly or indirectly with this project.

Firstly, I would like to thank my thesis supervisor Dr. ir. C.C.M. (Camilo) Rindt for his continuous guidance and helpful feedback throughout the project. I am grateful for being given the opportunity to complete this project with the Energy Technology Research group. I sincerely thank my coach Luca Scapino for his valuable support, weekly meetings, guidance, extreme patience and thesis report comments. It has improved the quality of the work and enhanced my research skills.

Secondly, I would like to thank Max Beving for his guidance and useful discussions throughout the project. Because of his expertise in the micro-scale investigation of thermo-chemical materials, the discussions have helped me to understand the performance of the material at micro-scale and then comparing it with reactor-scale. I am grateful for being able to perform this project made possible by Caldic (chemical company) by providing the K_2CO_3 composite sample for the reactor-scale investigation. During the project, continuous support was provided by the TFE lab staff. I would like to thank Jaap de Hullu (Laboratory Manager) for helping me improve the reactor design, Martin Huijzer for helping me in fixing the heater and pressure losses of the reactor, and Jan Hasker for helping me buying new thermocouples and heater.

Finally, I would like to thank my father (Abdul Razzaque), my mother (Rukhsana Bano) and my sister (Friha Razzaque) for their unconditional support and constant motivation during the project.

Abstract

The building sector accounts for almost 24% of the world's total CO_2 emissions [2]. There exists a great potential in reducing the CO_2 emissions from the building sector by integrating distributed energy sources. The intermittent nature of renewable energy sources leads to mismatch between the demand and supply needs. Sorption heat storage offers promising solutions to store surplus energy from renewables that could lead towards the transition of decentralized energy production. Thermo-chemical materials (TCMs) can store large amount of thermal energy due to a reversible chemical reaction.

In this project, a thermo-chemical material namely Potassium Carbonate (K_2CO_3) composite is used. It is provided by the chemical company Caldic, in the Netherlands. The sample consists of grains up to 3 mm. The K_2CO_3 composite is investigated experimentally on the reactor-scale setup. The aim of this project is to analyse the kinetic behaviour of K_2CO_3 composite at reactor-scale after consecutive sets of hydration and dehydration, and under variable operating conditions. A literature review is done to understand the current developments of sorption heat storage both on material and prototype level. The theoretical and experimental temperature lift in the reactor, the theoretical energy of the reactor and the energy density of the material are calculated.

The experiments are classified into two categories: cyclic and planned. The cyclic experiments are further divided into two phases and are performed with two different sets of operating conditions. Based on the amount of water absorbed during hydrations within a specified time duration, it is decided whether the sample has attained cyclability or not. The material is stabilized after phase 2 of cyclic experiments and the water content per cycle is improved. This is possibly due to the development of cracks after consecutive expansion and contraction of grains during reactions. Then, the material is used for the planned experiments to analyze the kinetic performance under variable operating conditions. In hydration, by increasing the water vapor concentration at reactor inlet, the water and energy released by the reaction is increased. By increasing the mass flow rate of air, the amount of water absorbed is reduced. By increasing the air temperature at reactor inlet, the material absorbed less water. This is because the material released the amount of water absorbed during hydration due to high inlet air temperature. In dehydration, by increasing the dehydration temperature and the mass flow rate of air at the inlet, the amount of water released is increased. It must be noted that in planned experiments, the alternative hydration and dehydration are performed at different operating conditions.

Contents

Nomenclature

A	Cross-sectional area	[m^2]
B	Thermocouple on inside reactor wall, Shape factor	[-]
C_p	Specific heat capacity	[J/(kg·K)]
C	Water vapor concentration	[mol/m^3]
D	Reactor inner diameter	[m]
d_p	Particle diameter	[m]
ΔG	Change in Gibbs free energy	[kJ/mol]
h	Convective heat transfer coefficient of air	[$W/(m^2 \cdot K)$]
H	Bed height	[m]
ΔH	Change in Reaction enthalpy	[kJ/mol]
k	Thermal conductivity of air	[W/(m·K)]
L	Reactor length	[m]
ΔL	Distance between bed position in reactor	[m]
$\dot{m}$	Mass flow rate	[kg/s]
M	Molecular mass	[kg/mol]
M	Thermocouple at the middle of reactor bed	[-]
Nu	Nusselt number	[-]
P	Pressure	[Pa, bar]
Pr	Prandtl number	[-]
P_{H_2O}	Water vapor pressure	[mbar]
Q	Dimensionless factor for non-equilibrium conditions	[-]
R	Universal gas constant	[J/(mol·K)]
R	Heat resistance	[$(m^2 \cdot K)/W$]
RH	Relative humidity	[%]
Re	Reynolds number	[-]
r_1	Reactor inner radius	[m]
r_2	Reactor inner radius + Teflon	[m]
r_3	Reactor inner radius + Teflon + Stainless steel	[m]
r_4	Reactor inner radius + Teflon + Stainless steel + Insulation	[m]
ΔS	Change in reaction entropy	[J/(mol·K)]
ΔT	Change in temperature	[°C]
T	Temperature	[°C], [K]
t	Layer thickness	[m]
u	Velocity of air entering the reactor	[m/s]
U	Overall heat transfer coefficient	[$W/(m^2 \cdot K)$]
V	Volume	[m^3]
W	Thermocouple on outside reactor wall	[-]

Greek symbols

ϵ	Porosity	[-]
ρ	Density	[kg/m^3]
λ	Thermal conductivity	[W/(m·K)]
μ	Viscosity	[Pa·s]

Abbreviations

CD	Case dehydration
CH	Case hydration
CEM	Controlled evaporator mixer
ECN	Energy research center
GFC	Gas flow controller
HYDES	High energy density sorption heat storage for solar space heating
LFC	Liquid flow controller
PCM	Phase change material
PD	Phase dehydration
PH	Phase hydration
RH	Relative humidity
SIM	Salt in matrix
SS	Stainless steel
SPF	Institut für Solartechnik
SWEAT	Salt water energy accumulation and transformation
TCM	Thermochemical material
WSS	Wakkanai siliceous shale
ZAE	Zentrum für Angewandte Energieforschung

Superscripts/Subscripts

a	Air
B	Inside reactor wall
b	Bed
cond	Conduction
conv	Convection
del	Deliquescence
eq	Equilibrium
ins	Insulation
in	Inlet
max	Maximum
out	Outlet
sat	Saturation
ss	Stainless steel
Th	Theoretical
tef	Teflon
v	Vapor
W	Outside reactor wall

Chapter 1 | Introduction

1.1 Energy Challenge

The significant advantage of integrating renewable energy sources in the current energy systems and power grids is their ability to mitigate carbon emissions and direct pollution [1]. With the increasing energy demand, fossil fuels have already been exploited to their maximum. To conserve the available limited natural resources, essential policy efforts are required to increase the use of renewable energy sources. The building sector is one of the largest energy-consuming sector, accounting for almost 24% of the world's total CO_2 emissions, 40% of the world's total primary energy consumption [2], of which 75% is consumed for domestic water heating and space heating [3]. In the Netherlands, 53.3% of the total primary energy consumption (450 PJ/year) accounts for space heating [4], as shown in Figure 1.1, which is attained mostly from natural gas. These statistics reveal that there exists a great potential in reducing the carbon emissions from the building sector and there is a need to focus on heat demand generation from renewable energy at residential and domestic level. Energy storage offers suitable solutions that could lead towards the transition of decentralized energy production, thereby attaining higher flexibility in balancing the demand and supply needs. Solar energy, as one of the most abundant energy source on earth accounting for more than 10,000 times the world's total energy use [5], could be harnessed on residential roof-tops to fulfil energy demands. The major challenge is the imbalance between the solar irradiation and heat demand in winter and summer seasons as shown in Figure 1.2. One of the possible solutions is to store surplus thermal energy during summers and use it in winters when the heat demand is higher.

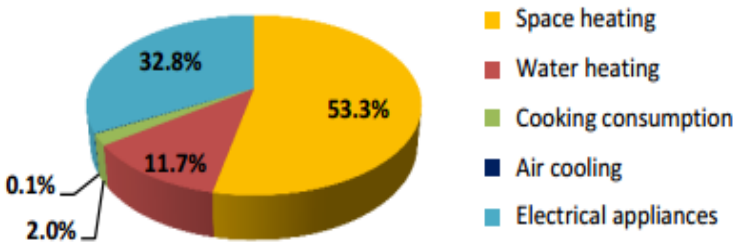

Figure 1.1: Primary energy consumption by end users, identified in the household of the Netherlands in 2009 [4].

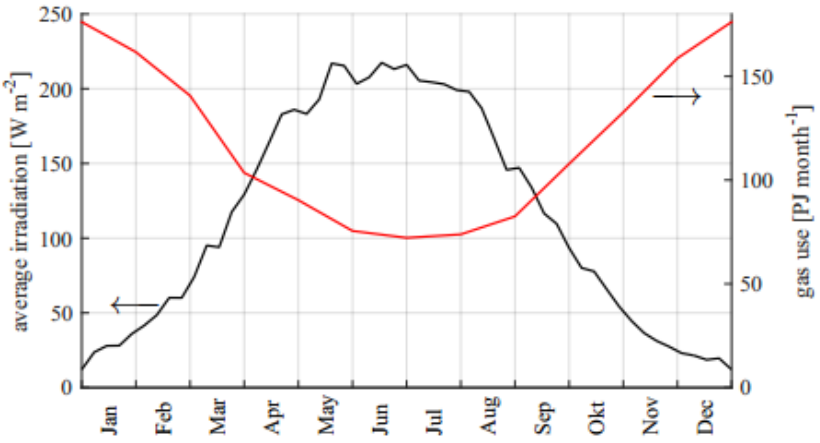

Figure 1.2: Solar irradiation per square meter [6] (average from year 1977 to 2015) and gas consumption [7] (average from year 2010 to 2015) in the Netherlands.

1.2 Thermochemical heat storage

For thermal energy storage, there are three fundamental categories: sensible, latent and sorption heat storage. For each storage concept, numerous materials have been investigated such as sensible heat storage material, phase change material (PCM) or thermochemical material (TCM). After extensive researches [8]–[10], there is still a gap to overcome the challenges of optimal energy density, heating power, operating cost, toxicity issues, and stability across different ranges of operating temperatures.

For sensible heat storage, the most prominent and commonly used material is water, which has numerous advantages including excellent mechanical and chemical stability, ease of availability, low cost and non-toxic nature. But on the other hand, research has highlighted a lower energy density of water i.e. 0.25 GJ/m^3 for a ΔT of 60 °C [11]. Despite several benefits of using water as storage material, there are challenges that may be solved by focusing on thermal insulation of water tanks and reducing major heat losses over time.

Another family of storage material is organic PCM, where majority of them offer thermal stability, appropriate mechanical and chemical properties but again the drawbacks of low energy density (0.2 GJ/m^3), combustive nature, low thermal conductivity (0.2 W/(m·°C)) [11] and economical concerns pose significant threats towards the development of using this material as a reliable storage source. Inorganic PCMs have a substantial potential of reducing the storage tank volume owing to its comparatively higher energy density (0.25-0.5 GJ/m^3) and thermal conductivity (0.3–0.6 W/(m·°C)) than organic PCMs and water [12]. There are still challenges with this storage material such as corrosion, phase segregation and sub-cooling. Research suggests that the rusting and lower thermal conductivity issues could be solved by implementing technical processes such as impregnation or encapsulation [11].

Thermochemical heat storage is a reversible physical-chemical reaction during which heat is either released or absorbed depending upon the direction of the reaction. Sorption heat storage also include thermochemical heat storage, despite of the fact if it's a chemical reaction or a physical adsorption reaction [13]. Sorption can be fundamentally classified into two types: sorption in liquids and sorption in solids. Sorption in liquids include the absorption of water vapor in hygroscopic salt solutions, whereas sorption in solids is further classified into physisorption and chemisorption materials. In physisorption (or physical adsorption), the sorption occurs at the external surface of the material without affecting the internal structure of the sorbent and is related to weak Van der Waals bonding. In chemisorption (or chemical absorption), the sorption occurs at the molecular level within the crystal lattice, thereby modifying the entire composition, geometry of the sorbent, and is related to chemical bonding. Compared to PCMs and water, all types of TCMs offer greater theoretical energy density in the range of 0.7–2.8 GJ/m^3 and have a significant advantage of almost loss-free heat storage over time. Additionally, TCMs have solved the problem of large storage volumes to considerable extent by reducing it to an order, where it can be suitable for domestic applications.

In thermochemical reactions, the TCM undergoes two basic cycles, hydration (exothermic reaction) and dehydration (endothermic reaction) as shown in Figure 1.3. During charging (dehydration), the sorbent splits into two components and heat is stored in the material due to an endothermic process. This stored heat from the material can be re-used later due to the possible reversible chemical reaction. The heat released due to an exothermic process during discharging (hydration), can be used for different domestic energy needs, such as domestic tap water heating (≤60 °C) and space heating (30–40 °C).

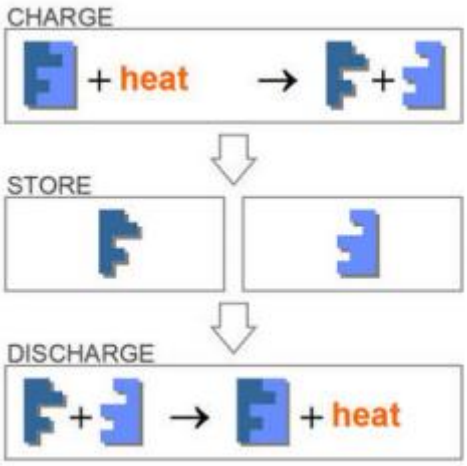

Figure 1.3: Charging (dehydration) and discharging (hydration) phenomena of a TCM

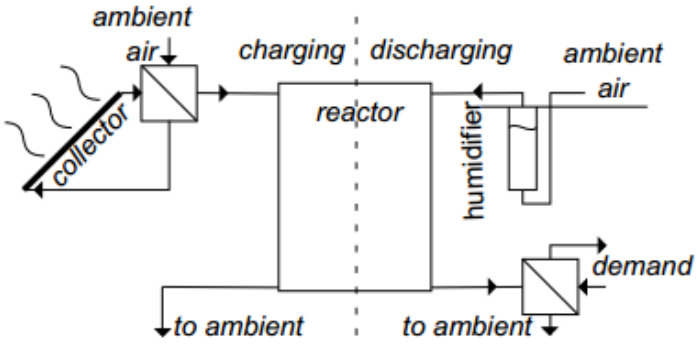

Figure 1.4: Open thermochemical heat storage system in real life application [14]

For better understanding of a thermochemical heat storage system, let's consider an example, as shown in Figure 1.4. During summers with the surplus amount of solar energy, solar irradiation can be used by solar collectors to heat up the air. The market already has solar heating system coupled with vacuum tube solar collectors, that has a capacity to achieve higher temperature ranges i.e. 120 °C–150 °C [15]. The heated air flows across the reactor and removes the water from the salt hydrate, as shown by Equation 1.1. The TCM is now charged and is ready to be used in winters, when the solar irradiation will be lower, and the heat demand will be higher. In winter, the ambient air can pass through the humidifier to add correct mixture of air and water to the reactor. The dried salt begins to absorb water and the heat is released during discharging. This released heat is used for domestic heating purposes by means of a heat exchanger.

$$Salt.xH_2O_{(s)} \rightleftharpoons Salt_{(s)} + x.H_2O_{(g)} \qquad \text{Equation 1.1}$$

1.3 Objectives and outline

To investigate the potential of thermochemical heat storage, there is a need to analyse the heat storage systems and the TCM stored in it. Although all the low temperature TCMs offer higher theoretical energy densities (0.7–2.8 GJ/m^3) compared to PCMs, but the challenges of charging losses associated with heat capacity (C_p) are still to be investigated. Liquid sorption, adsorption and absorption materials during different research projects showed promising factors required for domestic applications [16]–[18]. However, drawbacks of

material solidification, high cost and toxicity respectively, are major concerns for large-scale implementation. Water vapour sorption in crystalline salt hydrates showed greater potential as far as safety and non-toxicity of the thermochemical process is concerned. The initial experiments performed with this sort of material produced promising energy storage density (0.5–1.5 GJ/m^3 in a packed bed), that permitted substantial reduction in the size of storage tank of up to 10 m^3 [18]. Further in-depth research is needed to comprehend issues related to material stability, slow reaction rates and energy storage density.

The experiments are performed on reactor setup with potassium carbonate (K_2CO_3) composite as a storage material. The overall objective of this graduation project is to investigate a new heat storage composite material and its possibilities for thermo-chemical heat storage in the built environment. The material is provided by the chemical company Caldic, in the Netherlands and contains particles ranging up to 3 mm. To achieve the overall objective of research, following research questions are addressed:

1. What is the kinetic behaviour of the K_2CO_3 composite at reactor-scale after cyclic experiments of consecutive hydration and dehydration?

2. What is the kinetic behaviour of the K_2CO_3 composite at reactor-scale under variable operating conditions?

In Chapter 2, a literature review is done on a material level, which is currently being researched for a long-term sorption heat storage for short-range temperature (30 °C–150 °C) applications, such as domestic water heating, space heating and other industrial processes. Based on the literature review, reasons are provided for considering K_2CO_3 as the most suitable candidate for sorption heat storage for both open and closed systems. The chapter also includes a literature review on a prototype scale, thereby highlighting the challenges and issues with the storage materials in real life applications.

In Chapter 3, an introduction of the reactor setup is provided to understand the working principle of its components. A theoretical performance of the setup is estimated to realize how much reality differs from the theoretical expectations. A detailed experimental plan is discussed to comprehend the methodology followed in the experimental phase. Finally, reactor energy balance is done to estimate the amount of heat released/absorbed during hydrations and dehydrations respectively.

In Chapter 4, the results are discussed in detail for the two sets of cyclic experiments performed at two different operating conditions to observe the cyclability and kinetic performance of K_2CO_3 composite. The results of planned experiments are presented, which provide an insight into the kinetic behavior of the K_2CO_3 composite by varying controlled input parameters. An experimental performance of the setup is determined to compare it with the theoretical performance.

In Chapter 5, a detailed conclusion is presented to discuss how the material behaved during the experimental phase i.e. cyclic and planned experiments. Finally, guidelines and recommendations are listed to propose appropriate solutions to the challenges faced during the experimental phase.

Chapter 2 | Literature Review

Sorption heat storage includes both physical and chemical bonding for heat storage. Extensive research is being made for its long-term applications [19]–[22]. N'Tsoukpoe et al. [20] reviewed the state-of-the-art in long-term sorption heat storage materials and technological difficulties; Xu et al. [19] reviewed the development of sorption materials and proposed sorbents for heat storage; and Scapino et al. [23] reviewed the latest advancements on sorption storage technologies for long-term low-temperature applications. A literature review is done to understand the current developments of sorption heat storage both on material and prototype level. It provides an overview of the performance of potential sorption materials and possible challenges with their storage. This graduation project is focused on K_2CO_3 composite; therefore, it is important to realize the characteristics of pure K_2CO_3 such as chemical behavior in sorption storage applications. Finally, a discussion of why it is considered a suitable candidate for sorption heat storage, is presented.

2.1 Material level

This section provides an overview of the recent research performed on sorption heat storage at material level with water as sorbate. The salt hydrates and composite materials are examined to reduce the list of options available for sorption heat storage. These storage materials offer suitable properties such as low cost, ease of availability and safety. However, challenges such as deliquescence, agglomeration and melting issues at ambient conditions, make it difficult to use them in ordinary operating conditions. Before in-depth analysis of materials, it is important to know the classification of sorption heat storage. According to Yu et al. [19] there are four basic divisions for sorption reactions: solid adsorption, liquid absorption, chemical reaction and composite materials. For the sake of interest and relevance to this project, only chemical reaction materials and composites are discussed.

2.1.1. Salt hydrates

In chemical reaction materials, salt hydrates are discussed to realize their properties suitable for long-term heat storage. Recently, salt hydrates are of interest for thermal storage purposes due to their high effective energy density and suitable final temperatures for residential applications. Van Essen et al. [24], [25] investigated hydration and dehydration reactions for $MgSO_4.7H_2O$ at 13 mbar and found that at 52.5 °C, large particles (>200 μm) begin to melt for heating rates higher than 1 °C/min. It was concluded that only discharge temperatures below than 50 °C are appropriate for this material. Ferchaud et al. [26], [27] analyzed the molecular structure, during the dehydration reaction, in two distinct steps i.e. at 30–45 °C and 60–75 °C ($MgSO_4.2H_2O$) respectively. However, for attaining monohydrate $MgSO_4$, a higher desorption temperature of 150 °C at 13 mbar water vapor pressure was required. Further analyzing the reaction kinetics, Ferchaud [28] concluded that $MgSO_4$ is not suitable for seasonal heat storage owing to its slow reaction rates. This challenge could be overcome by raising the water vapor pressure to 50 mbar with the constant temperature of 36 °C to prevent over-hydration. Donkers et al. [29] studied the cyclic performance of $MgSO_4$ and found the formation of pore water within the crystal lattice, which ultimately reduces the material performance over time. Brunberg et al. [30], [31] performed primary research on Na_2S to comprehend the material heat storage potential and proved it by practically implementing it on different prototype projects. De Boer et al. [32], [33] suggested Na_2S as a space cooling material and analyzed its dehydration at 17 mbar, which takes place in two separate steps, at 49 °C followed by 60–100 °C. Trausel et al. [34] highlighted the challenges of using Na_2S as storage material such as corrosive nature and formation of toxic H_2S. Van Essen et al. [35] investigated $MgCl_2.7H_2O$ and

observed that heating rate higher than 1 °C/min during experiments resulted in sample melting. To avoid this situation, a constant heating rate of 1 °C/min was used. During the dehydration of $MgCl_2.6H_2O$, HCl is formed due to the hydrolysis of magnesium chloride di-hydrate. This HCl formation is a major drawback for the built environment because it is unsafe to deal with in practical conditions. Bertsch et al. [36] performed experiments using $CuSO_4$ as sorption heat storage material and found the powder of crystals due to extensive expansion/contraction associated with hydration/dehydration reactions. The toxic nature adds hindrance in the material application for domestic purposes. Michel et al. [37] found strontium bromide as the most promising candidate for sorption heat storage owing to its lower dehydration temperature i.e. 80 °C. Moreover, it offers a higher energy density of 1.44 GJ/m^3 [37] and demonstrated stability over multiple cycles during prototype experiments [38]. The major drawback is the high price, which makes it difficult to use on a large commercial scale.

2.1.2 Composites

Despite numerous useful characteristics of salt hydrates, there are still challenges which slowed down their large-scale implementation for sorption heat storage purposes. These include deliquescence at a lower temperature, melting at a higher temperature, cracking upon extreme cycling rates, lower energy densities and thermal conductivity [23]. The composite materials can overcome these challenges. They have gained significant attention due to their structural composition and characteristics. They basically consist of two materials: active material and inert material. The addition of inert material might result in decreasing the energy density of the material. Conversely, it might result in enhancing other important properties such as material stability. Hence, a trade-off must be done with the use of composite materials to provide for the structural stability.

Casey et al. [39] developed a Salt in matrix (SIM) to classify hygroscopic salts as materials suitable for open thermal energy storage systems. The salts selected include $CaCl_2$, $MgSO_4$, $Ca(NO_3)_2$, $LiNO_3$ and LiBr, whereas silica gel, zeolite, activated carbon and vermiculite, were selected as matrices. The objective was to reduce different combinations to obtain suitable candidates by developing some sort of selection criteria. The author found vermiculite with LiBr or $CaCl_2$ as a suitable candidate for showing higher sorption heat storage potential. To overcome the drawbacks of salt hydrates, Druske et al. [40] integrated optimized mixer of $CaCl_2$ with K_2CO_3 and impregnation of $CaCl_2$ in matrices as activated carbon foam or expanded natural graphite. The obtained composite material showed enhanced hydration and dehydration behaviour, energy density and thermal conductivity. Liu et al. [41] synthesized a composite made up of mesoporous Wakkanai siliceous shale (WSS) and LiCl experiment in an open sorption storage system. The addition of LiCl in the mesopores of WSS enhanced the sorption capacity, stability and cyclability of the composite. Opel et al. [42] combined $MgCl_2.6H_2O$ with graphite, copper, zeolite and sand to synthesize a composite material and found that thermal conductivity was increased with graphite.

2.1.3 Properties of K_2CO_3

This section highlights the characteristics of pure K_2CO_3 such as chemical behavior in sorption storage applications. The K_2CO_3 is a white odorless powder that exists in two different states, namely anhydrate and sesquihydrate (1.5 H_2O). The latter has small white translucent crystals, which has an equilibrium relative humidity (RH) of 43% at an equilibrium temperature of 20 °C [43]. RH of 43% corresponds to a water vapor pressure (p_{H_2O}) of 0.01 bar at 20 °C, as shown by the green line in the phase diagram of K_2CO_3 (Figure 2.1). The challenge with the sesquihydrate state is the risk of deliquescence under ambient conditions. This implies that storage of sample is crucial for material safety. The K_2CO_3

exhibits a reversible reaction with a moist air interaction, given by Equation 2.1, which is of main interest for TCM applications. This reversible reaction is a single step reaction, which leads to a simple kinetic mechanism. The reaction oscillates between the two states depending upon the operating conditions. Upon heating, sesquihydrate loses water molecules and transforms to anhydrous state and vice versa.

$$K_2CO_3.1.5\,H_2O(s) \rightleftharpoons K_2CO_3(s) + 1.5\,H_2O(g) \qquad \text{Equation 2.1}$$

2.1.3.1 Phase Diagram of K_2CO_3

The vapor curve shows the equilibrium pressure between liquid water and water vapor at a given temperature [44]. For salt hydrates, vapor curve provides an equilibrium between water vapor and water absorbed in the salt. The phase diagram (Figure 2.1) is formed by determining the equilibrium curves of H_2O and K_2CO_3 from the values of formation of enthalpy and entropy of reaction. The values used for formation enthalpy and entropy at standard conditions for H_2O and K_2CO_3 are present in Appendix A. The change in Gibbs free energy (ΔG) indicates the direction of reaction i.e. if positive, the reaction is spontaneous, if negative, the reaction is non-spontaneous and if zero, the process is in chemical equilibrium. The equilibrium temperature for a given water vapor pressure (p_{H_2O}) can be calculated assuming $\Delta G = \Delta G^0 + RTlnQ = 0$ (imposing chemical equilibrium under standard conditions) and is given by Equation 2.2.

$$T = \frac{\Delta H}{\Delta S - RlnQ} \qquad \text{Equation 2.2}$$

Whereas, ΔH and ΔS are enthalpy and entropy change of a reaction respectively. These can be calculated from the formation enthalpies and the standard molar entropies of the materials involved in the reaction. Q is a dimensionless factor for non-equilibrium conditions with all pressures in bar and is given by Equation 2.3.

$$Q = \frac{P_{product1} \times P_{product2}}{P_{reactant1} \times P_{reactant2}} \qquad \text{Equation 2.3}$$

Similar methodology (Equation 2.2) is adopted for calculating the equilibrium curve of K_2CO_3. After calculating the equilibrium temperatures of H_2O and K_2CO_3, it is plotted against p_{H_2O} (bar) vector between 0.0001–1.5 in MATLAB software [45]. For the deliquescence line of K_2CO_3, equilibrium pressure of deliquescence line is calculated by Equation 2.4. It is then plotted against the K_2CO_3 deliquescence temperature (T_{del}) vector considered between 0–100 in MATLAB software.

$$p_{H_2O} = \frac{RH}{100} \times P_{sat} \qquad \text{Equation 2.4}$$

Whereas RH is the relative humidity, which is calculated by the method of least squares (Equation 2.5) based on the experimental data [43]. P_{sat} is the saturation pressure, which is calculated by Antoine Equation 2.6, to determine the maximum amount of water that the air can hold.

$$RH = \sum_{i=0}^{1} A_i T_{del}^i \qquad \text{Equation 2.5}$$

$$P_{sat} = exp(A - \frac{B}{C + T}) \quad \text{Equation 2.6}$$

Where A, B and C are the constants for Antoine equation valid for a maximum of 100 °C temperature.

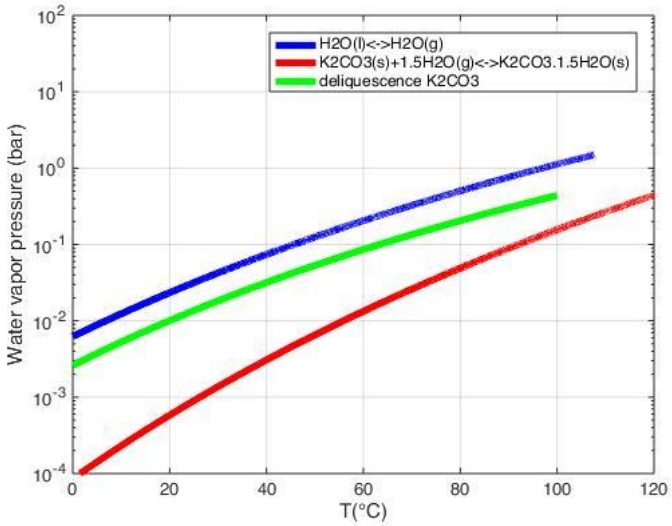

Figure 2.1: The phase diagram of K_2CO_3

The phase-diagram of K_2CO_3 provides information about the thermodynamic equilibrium properties such as water vapor pressure and equilibrium temperature, to regulate reactions under desired operating conditions. It also assists in keeping the material within the safe-zone during hydrations. A safe-zone is the region between the deliquescence line (green line) and $K_2CO_3.1.5H_2O$ (red line) during hydration as shown in Figure 2.1. If the safe-zone is breached, the material will reach the deliquescence state.

2.1.3.2 State of Hydration of K_2CO_3

The state of hydration determines the number of water molecules absorbed within the crystal lattice of K_2CO_3, sometimes also called as loading. It can be calculated by Equation 2.7, where $M_{K_2CO_3}$ and M_{H_2O} represent the molar masses of K_2CO_3 and water respectively. Similarly, $m_{K_2CO_3}$ and m_{H_2O} represent the anhydrous mass of K_2CO_3 and mass gain of water due to transition from anhydrous to sesquihydrate state. K_2CO_3 only has water molecules ranging between 0–1.5, therefore, if hydration is desired, the conditions must be maintained between K_2CO_3 deliquescence (green line) and $K_2CO_3.1.5H_2O$ (red line) as shown in Figure 2.1.

$$Loading\left[\frac{mol_{H_2O}}{mol_{K_2CO_3}}\right] = \frac{m_{H_2O} \times M_{K_2CO_3}}{m_{K_2CO_3} \times M_{H_2O}} \quad \text{Equation 2.7}$$

2.1.3.3 Reason for selecting K_2CO_3

A literature review of numerous salt hydrates is done to evaluate the thermodynamic data and ultimately justifying the selection of K_2CO_3 as a sorption heat storage active material. Donkers et. al. [46] proposed two sets of thermodynamic conditions for narrowing down the salt hydrate choices. Subsequently, further filtering is done based on other binding conditions such as price, safety and cyclic stability. Selection criteria for filtering out bulk of salt hydrates is shown in Table 2.1.

Donkers et al. [29] analysed an extensive data of 563 salt hydrates out of which 397 entries had the information of energy densities. With the binding hydration and dehydration temperature limitations in filter 1, only 165 and 415 salts were short-listed respectively. However, considering all the selection criterion of filter 1, 563 entries were reduced to only four, namely Na_2S, LiCl, $EuCl_3$ and $GdCl_3$. Furthermore, $EuCl_3$ and $GdCl_3$ are rare earth metals, which implies minimal chances of applying them on the large commercial scale due to cost constraints. Also, LiCl is corrosive and expensive [47], whereas Na_2S pose a risk of releasing H_2S gas [48], which is considered as a threat in the built environment sector. Applying the conditions of filter 2, 25 hydration reactions were short-listed. After analysing all the salt hydrates based on filter criterion, material price, cyclic stability and safety, K_2CO_3 is regarded as the most suitable candidate for sorption heat storage for both open and closed systems. It has an energy density six times higher than water on a material level with a ΔT of 50 °C and an exceptional quality of long-term heat storage. Lower dehydration temperature facilitates solar or waste heat recovery systems to deliver the temperature suitable for applications such as domestic hot water or space heating. Lower dehydration temperature also leads to lower output temperature, which may require additional heating to reach an appropriate temperature for the above-mentioned applications. K_2CO_3 owing to its lower dehydration temperature permits multiple cycles per year. Despite these advantages, there are still some challenges with K_2CO_3, such as for cyclic operations, the quantity of heat stored is reduced for each successive cycle. Moreover, the lower energy density (1.3 GJ/m^3) of pure K_2CO_3 offers a great potential to inspect K_2CO_3 composites further to remove this drawback and to find the optimal properties for seasonal heat storage. The current project is done to understand the issues of K_2CO_3 composite related to material stability, cyclability, reaction kinetics and energy storage density.

Table 2.1: Selection criteria for selecting suitable salt hydrate [46]

	Thermodynamic Conditions		Non-thermodynamic Conditions
Criteria	Filter 1	Filter 2	
Hydration reaction capacity	> 2 GJ/ m^3	> 1.3 GJ/ m^3	Price
Hydration temperature	65 °C or higher	50 °C or higher	Safety
Dehydration temperature	< 100 °C	< 120 °C	Cyclic stability

2.2 Prototype level

Sorption heat storage systems are not broadly implemented due to the issues of storage materials. These problems limit their large-scale applications. There are some projects of current sorption systems suitable for low-temperature applications. This section provides a brief overview of those prototypes and projects to comprehend the real-life application of sorption heat storage. The projects are classified as open and closed systems.

2.2.1 Open Systems

An open system is the one that exchanges both mass and energy with the environment i.e. the active sorbate is in direct contact with the sorbent but it also leaves the system, as shown in Figure 2.2. In a real-life system, the heat is extracted from the solar collectors, and hot air is then flown through the sorption bed to charge the material. The sorbent gets dried by losing water vapors, which are then released into the ambient. In ideal situation, if the dry sorbent is isolated from the moist air contact during storage period, the heat can be stored for long time without any thermal losses. For discharging process, the moist air (from

underground cold source) is flown through the sorption bed to discharge the material, which generally requires auxiliary energy such as fan. The dry sorbent combines with the water vapors, thereby releasing heat which is ultimately used for domestic household applications i.e. space heating and hot tap water. One of the advantage of an open system is the requirement of lower auxiliary energy during discharging, unlike fluidized or screw bed reactors. However, this reactor design can lead to lower energy densities due to the creation of non-reactive zones within the reactor.

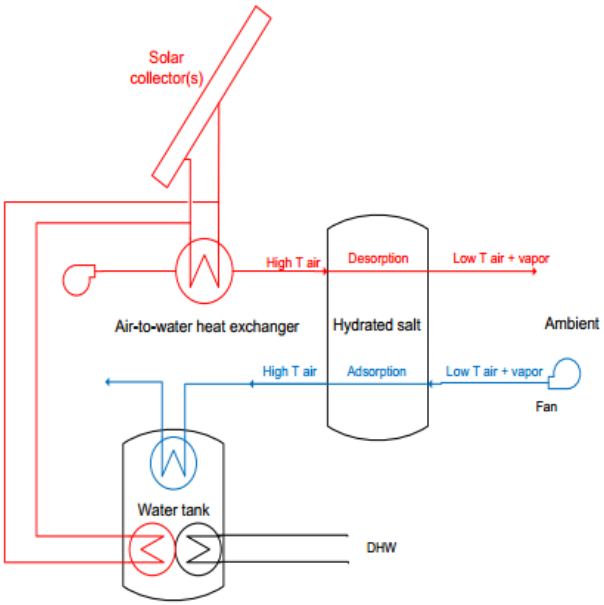

Figure 2.2: Open sorption system (red & blue line represents the charging & discharging cycles respectively) [49]

ZAE Bayern [50] built the foremost and largest prototype in Munich with the aim to offset the heating load of a school in summer and the cooling load of a club in winter. The sorption heat storage material used in the prototype is zeolite 13X. In the MonoSorp project, Bales et al. [51] demonstrated space heating of buildings by using zeolite 4A honeycomb storage material. The institute fuer Solartechnik SPF [51] performed a laboratory-based experiment with zeolite 13X as the active material and obtained 0.8 kW of discharge power. In ECN project, Zondag et al. [52] investigated $MgCl_2.6H_2O$ in a reactor based experiments and found that the material can be used for seasonal storage due to a good temperature rise of 20 °C. Mette et al. [13] in the project of CWS-NT/ITW used a composite of zeolite 13X and LiCl and compared to pure zeolite. With the composites, 20% higher discharge temperatures were obtained.

2.2.2 Closed Systems

A closed system is the one that exchanges only energy with the environment i.e. the active sorbate does not leave the system, as shown in Figure 2.3. In a real-life system, during the charging process, the absorbed vapor from the sorbent is condensed into a separate container rather than releasing into the ambient. The transport of sorbate occurs by the vapor pressure difference between the two containers i.e. evaporator/condenser and the sorbent bed. This implies that auxiliary energy is not required, unlike open system, to facilitate the vapor flow.

HYDES (High Energy Density Sorption Heat Storage for Solar Space Heating) project was initiated from 1998-2001 in which silica gel was used as an active material and energy density obtained was 0.43 GJ/m^3 [53]. In MODESTORE project, Jahnig et al. [54] tested silica gel with a spiral heat exchanger and concluded that it is not feasible for long-term sorption heat storage applications due to its bad thermal conductivity. De Boer et al. [33] used the Na_2S-H_2O working pair for sorption storage in SWEAT (Salt Water Energy Accumulation and Transformation) project.

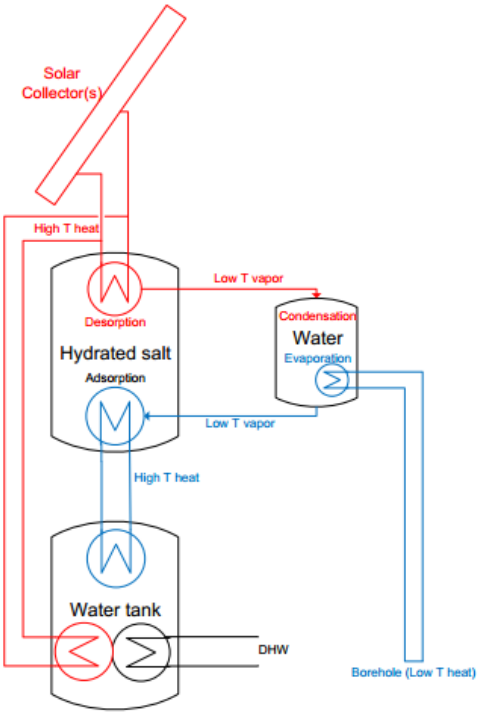

Figure 2.3: Closed Sorption System (red & blue line represents the charging & discharging cycles respectively) [49]

Chapter 3 | Reactor Design

3.1 Experimental Setup

A packed bed open reactor design is used for the experimental phase. The reactor setup has two independent paths: one for hydration and the other for dehydration, as shown in Figure 3.1. The compressor delivers the air at 7.5 bar with a relative humidity (RH) of 2.5% at 25 °C. During dehydration, the airflow to the reactor is regulated by the Gas Flow Controller (GFC). During this charging process, the heater increases the air temperature desired at the reactor inlet. In real life application, the heater function is performed by heat sources such as solar collectors, to dehydrate the material and store heat. Alternatively, during hydration, the airflow to the reactor is regulated by the GFC, the LFC (Liquid Flow Controller) and the CEM (Controlled Evaporator Mixer). The last two controllers regulate a controlled amount of air and water from the water vessel, to produce a mixture of air and water vapor. This moist air flows through the reactor bed to discharge the material and release heat. During dehydration, the cooling circuit is turned on to lower the air temperature that leaves the reactor before it reaches the RH sensor. The working range of the RH sensor is between -40°C to 80 °C [55]. Hence, it is essential to turn on the cooling circuit for accurate measurements of outlet RH. Otherwise, it may lead to measurement errors. The water is constantly moving in and out of the cooling circuit to extract the sensible heat from the hot air to water. The water flow in the cooling circuit is regulated by a valve at the bottom of the cooling circuit. The following section describes a brief explanation of major reactor setup components.

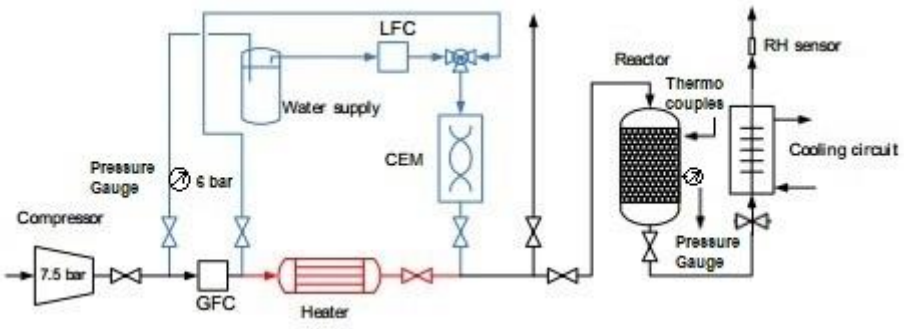

Figure 3.1: A scheme of reactor setup [14]

3.1.1 Reactor

The reactor bed has a cylindrical structure, with an inner and outer shell made up of Teflon and stainless steel (SS-316), respectively. The Teflon is used due to its lower thermal conductivity, which is required to retain the heat within the reactor by reducing the thermal losses. Also, to further reduce heat losses, a layer of glass-wool is wrapped around the reactor walls. A filter made up of sintered material with a pore size of 8 µm and a thickness of 5 mm, is placed at the bottom of the reactor to prevent K_2CO_3 composite grains to fall. The reactor has two valves, one at each end i.e. inlet and outlet. When the experiment is done, these valves must be closed to prevent the ambient air flow to the reactor, particularly after hydrations. The contrary may result in deliquescence of K_2CO_3 composite. Recent modifications are also made to make sure that the reactor is completely airtight. A pressure gauge is also attached to the reactor wall to monitor the inside reactor pressure during experiments.

3.1.2 Water Vessel

A pressure of 6 bar is set by a pressure gauge to ensure the pressure gradient, which serves as a driving force for the water to flow from the water vessel to the LFC. A water vessel is designed based on a conventional water pipeline network, which is made up of stainless steel, welded on each side with squared flanges. It is always filled with distilled water to prevent congestion issues inside the CEM heating part. Before hydrations, the water level must be at least three-quarters of the height of the water vessel. A schematic of the water vessel is shown in Figure 3.2.

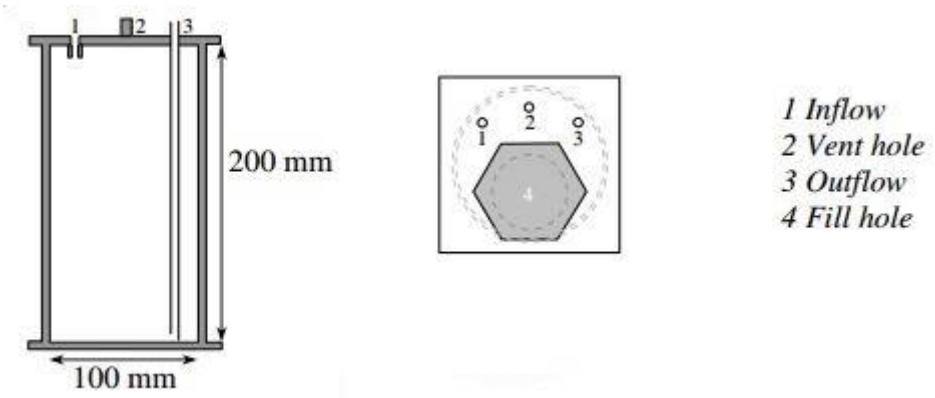

Figure 3.2: A scheme of the water vessel to supply water to LFC during hydrations [56]

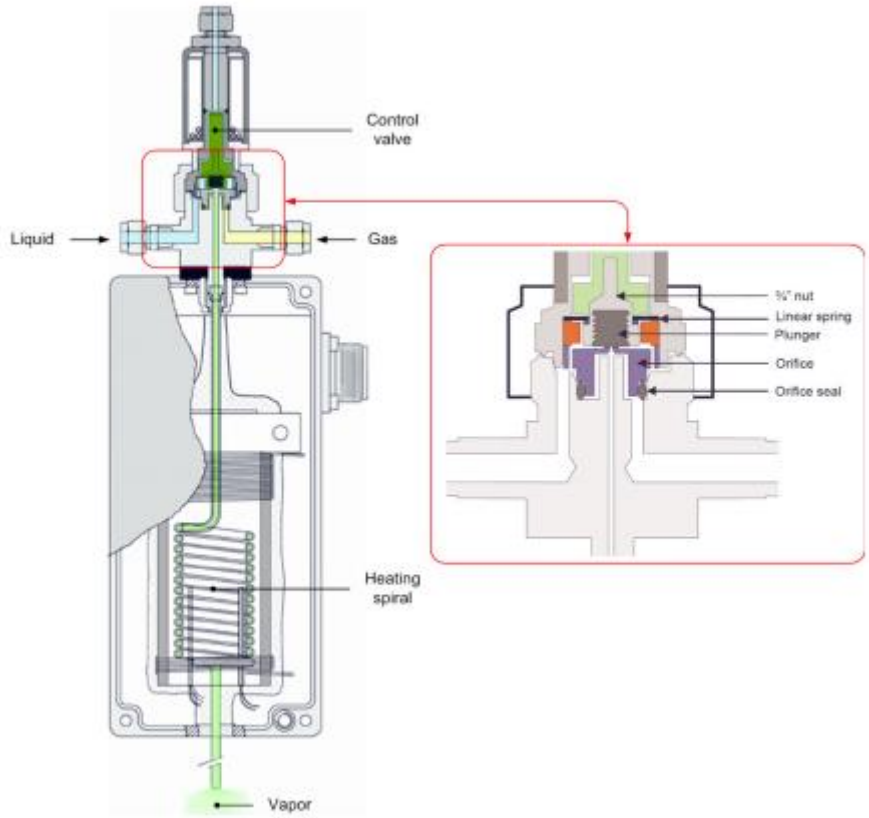

Figure 3.3: A schematic view of a controlled evaporator mixture [56]

3.1.3 Controlled Evaporator Mixer

The Bronkhorst® controlled evaporator and mixing system is used to regulate a suitable amount of air and water flows before passing the mixture to a heating element. The CEM

module is divided into two main components: mixing part and heating part. The former is made up of a control valve and a connection between air and liquid. It ensures a suitable amount of liquid flow, which is regulated by a small orifice (100 µm) controlled by a spring plunger. The plunger in its neutral position remains closed but owing to the presence of an electromagnetic force, plunger opens which allows liquid flow through the orifice. The orifice is a critical part because it is responsible to generate small water droplets by means of the carrier air flow, which is present under the small orifice. The water droplets and carrier air form a mixture, which is ready to enter the heating part. The mixture flows through the spiral tubes, where the temperature is controlled externally and can be varied. The outcome is a mixture of air and water vapor, which is considered stable and accurate. A schematic view of CEM is shown in Figure 3.3.

3.1.4 Heater

During dehydration, a 400W electrical heater is used to heat up the incoming compressed air regulated by GFC. The heater must be turned on if there is an airflow through it. The contrary can result into a burn-out heater. The heater operation is controlled by the Bronkhorst® software, where the ramping rate for heating is set as 1 °C/min until the maximum desired temperature. After that, the heater continues to deliver the air at that maximum temperature according to the set program. The thermocouples are positioned at three different locations (Figure 3.4) to measure:

- the temperature of the air leaving the heater (Thermocouple 1)
- the heater wall temperature (Thermocouple 2)
- the temperature of the air leaving the blow-off valve (Thermocouple 3)

A control system is designed to shut-off the heater in two conditions. Firstly, if there is no air flow through the heater. Secondly, if the heater wall temperature (T2) shown by the thermocouple is above the set heater wall temperature in the software. Due to heat losses, there is a temperature difference between the air leaving the heater and air entering the reactor inlet.

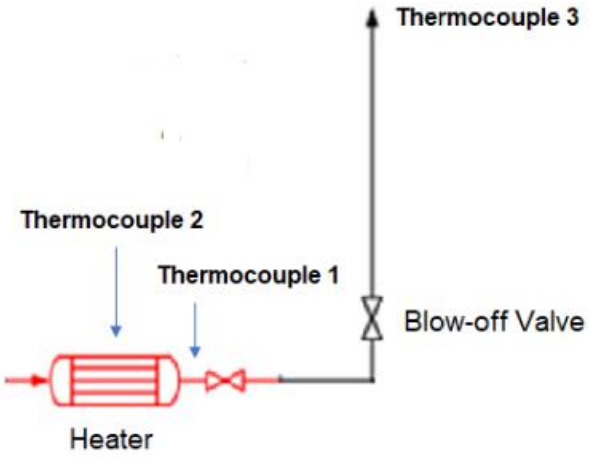

Figure 3.4: A scheme of thermocouple locations for the heater

3.1.5 Thermocouples

To monitor the temperature profile during the reactor operation, thermocouples are placed at 17 different locations as shown in Figure 3.5. The thermocouples are positioned at five different heights (h = 90, 70, 50, 30, 10 mm), and three various radii i.e. in the middle, inside and outside surface of the reactor, named as M (r = 0 mm), B (r = 35 mm) and W (r = 52.5

mm) respectively. Two types of thermocouples are used: K-type and T-type. The former ones are attached to the wall, W1–W5, with an accuracy of ±1%. The later ones are attached inside the reactor, M1–M5, B1–B5, T_1 and T_2, with an accuracy of ±0.5%. A humidity and temperature sensor are placed after the cooling circuit to measure the humidity and temperature of the outlet air. The thermocouples are also tested (see Appendix B).

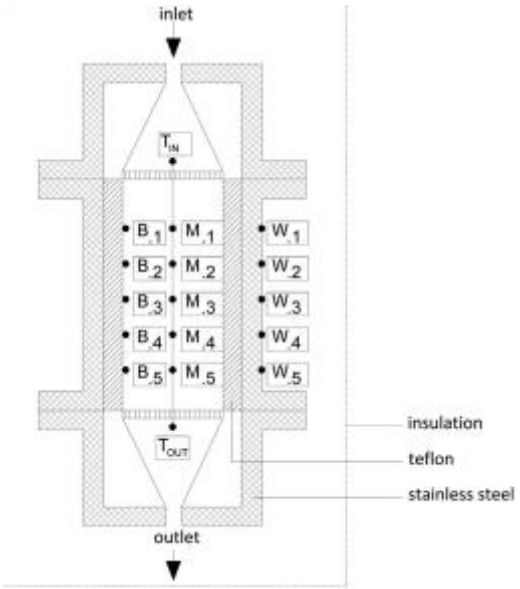

Figure 3.5: A scheme of thermocouple locations at five different heights (1-5), i.e. on outside wall (W), on inside wall (B) and in the middle of the reactor bed (M) [14]

3.2 Methodology and Experimental Plan

This section includes the theoretical performance of the reactor setup to compare it with the experimental performance. Prior to experiments, the K_2CO_3 composite is prepared to make the sample ready for hydration and dehydration. The detail of the sample particle size distribution is listed, followed by the methodology adopted to investigate the kinetic performance of K_2CO_3 composite during hydration and dehydration.

3.2.1 Theoretical Setup Performance

3.2.1.1 Theoretical Temperature Lift in the Reactor

The theoretical temperature lift in the reactor is calculated to realize how much reality differs from the theoretical expectations. In an open system, there are two methods to approximate the maximum temperature rise in the first order.

Method 1: For high values of reaction enthalpy (ΔH), 'C_p air approximation' method can be used to estimate the temperature step. Certain assumptions are considered, such as all the sorbate is completely absorbed by the sorbent, there are no thermal losses and the entire heat released by the sorbent is utilized to heat up the air. It must be noted that higher temperature lift in an open system can be obtained by using higher vapor pressure. The theoretical temperature rise of the current reactor setup is calculated by Equation 3.1 for the reference hydration performed according to the operating conditions mentioned in Table 3.1.

$$\Delta T = \frac{C_{in}\,\Delta H}{\rho_{air}\,C_{p_{air}}} = \frac{0.3\,\frac{mol}{m^3} \times 63.6\,\frac{kJ}{mol}}{1.225\,\frac{kg}{m^3} \times 1\,\frac{kJ}{kg.°C}} = 15.5\ °C \qquad \text{Equation 3.1}$$

For the reference hydration, inlet air temperature (T_1) is known i.e. 25 °C. Hence, the theoretical outlet air temperature (T_2) can be calculated by Equation 3.2.

$$T_2 = T_1 + \Delta T = 41\ °C \qquad \text{Equation 3.2}$$

Method 2: For low values of ΔH, the equilibrium temperature is calculated to determine the maximum temperature rise in the first approximation. The equilibrium temperature (T_{eq}) for a reference hydration (Table 3.1) is calculated by following a method as mentioned above (in section 2.1.3.1) and is given by Equation 3.3.

$$T_{eq} = \frac{\Delta H}{\Delta S - RlnQ} = 52\ °C \qquad \text{Equation 3.3}$$

Also, the maximum temperature rise can be calculated by Equation 3.4.

$$\Delta T = T_{eq} - T_1 = 27\ °C \qquad \text{Equation 3.4}$$

In first order approximation, the maximum temperature rise in an open system is given by the lowest ΔT value calculated from the two approximation methods. Hence, the theoretical temperature lift for the current reactor setup is 16 °C with a corresponding outlet air temperature of 41 °C.

3.2.1.2 Theoretical Energy Density of the Reactor

The theoretical energy density of the reactor is calculated by considering the reactor bed porosity. A particle density of sesquihydrate K_2CO_3 is 2180 kg/m³ and molar weight of the anhydrous K_2CO_3 is 138 g/mol. From literature, the absorption enthalpy of K_2CO_3 is 63.6 kJ/mol [57]. It is known that sesquihydrate K_2CO_3 can take up to 1.5 moles of water, therefore, the resulting molecular weight of sesquihydrate K_2CO_3 can be calculated as:

$$M_{K_2CO_3} = 138\frac{g}{mol} + 1.5\ mol\ H_2O \times 18\ \frac{g}{mol} = 0.165\ \frac{kg}{mol}$$

So, 1 m³ of sesquihydrate K_2CO_3 can store:

$$Energy\ density\ (with\ \epsilon_b = 0) = \frac{2180\ \frac{kg}{m^3}}{0.165\ \frac{kg}{mol}} \times 1.5\ mol\ H_2O \times 63.6\ \frac{kJ}{mol} = 1.26\ \frac{GJ}{m^3}$$

This is the energy density assuming that all the volume in the reactor is occupied by the salt ($\epsilon_b = 0$). But the reactor has certain bed porosity, which is calculated by Equation 3.5.

$$\epsilon_b = 1 - \frac{\rho_{bed}}{\rho_{particle}} = 1 - \frac{\left(\frac{m_{K_2CO_3}}{V_{K_2CO_3}}\right)}{\rho_{particle}} \qquad \text{Equation 3.5}$$

$$\epsilon_b = 1 - \frac{\left(\frac{0.42\ kg}{4.23 \times 10^{-4}\ m^3}\right)}{2180\ \frac{kg}{m^3}} = 0.54$$

Now, the real theoretical energy density including the bed porosity is:

$$Energy\ Density\ (with\ \epsilon_b = 0.54) = 1.26\ \frac{GJ}{m^3} \times (1 - 0.54) = 0.6\ \frac{GJ}{m^3}$$

3.2.1.3 Theoretical Energy of the Reactor

The theoretical energy content of the reactor is obtained simply by multiplying the energy density of K_2CO_3 with the reactor volume (considering the reactor bed porosity).

$$Theoretical\ Energy\ of\ reactor = 0.6\ \frac{GJ}{m^3} \times 4.23 \times 10^{-4}\ \mathrm{m}^3 \times (1 - 0.54) = 132\ kJ$$

3.2.1.4 Theoretical Overall Heat Transfer Coefficient

The overall heat transfer coefficient (U) is calculated to determine the heat transfer across the reactor wall. Figure 3.6 shows a schematic view of the reactor model in which the temperature calculations are expressed in the vertical direction (z-coordinate) and heat resistances are connected in the radial direction. The reactor wall is composed of three different layers: the inner is made up of Teflon of 75 mm, the middle is made up of stainless-steel (SS-316) of 10 mm, and the outer is made up of glass-wool insulation of 30 mm.

The rate of heat transfer through the reactor wall is calculated in Equation 3.6.

$$\sum_{i=1}^{5} \left(\frac{T_{Bi} - T_{Wi}}{R}\right) A_w \qquad \text{Equation 3.6}$$

Where T_B is the Teflon inner wall temperature and T_W is the outer stainless-steel wall temperature (Figure 3.6). R is the heat resistance at the inner and outer sides of the wall given by Equation 3.7. It is a summation of the convective heat resistance at the inside wall between air and Teflon layer (R_{conv}), conductive heat resistance in the Teflon layer ($R_{cond,tef}$), stainless-steel layer ($R_{cond,SS}$) and glass-wool insulation layer ($R_{cond,ins}$). The convective heat resistance at the outside surface of the insulation layer is neglected.

$$R = (R_{conv} + R_{cond,tef} + R_{cond,ss} + R_{cond,ins})A_w \qquad \text{Equation 3.7}$$

$$R_{Th} = \left(\frac{1}{2\pi r_1 Lh} + \frac{\ln\left(\frac{r_2}{r_1}\right)}{2\pi\lambda_{tef}L} + \frac{\ln\left(\frac{r_3}{r_2}\right)}{2\pi\lambda_{SS}L} + \frac{\ln\left(\frac{r_4}{r_3}\right)}{2\pi\lambda_{ins}L}\right) A_w = 0.11\,\frac{\mathrm{m}^2 \cdot K}{W}$$

Where, r is the radius, L is the reactor length, λ is the thermal conductivity of materials, A_w is the cross-sectional area of the body of the reactor and h is convective heat transfer coefficient, which is explained in detail in Appendix C. The values of all the parameters involved in the calculation of heat resistance (R) are shown in Appendix H. The overall heat transfer coefficient is simply the reciprocal of the heat resistance and is calculated by Equation 3.8. The higher value of U shows that the reactor walls have less resistance to heat flow or they do not have good insulating properties. One of the possible reason for higher value of U calculated below, is due to higher thermal conductivity (λ) of stainless steel. It is the property of a material to conduct heat and higher value of λ means poor insulating properties.

$$U_{Th} = \frac{1}{R} = 9\ \frac{W}{m^2 \cdot K} \qquad \text{Equation 3.8}$$

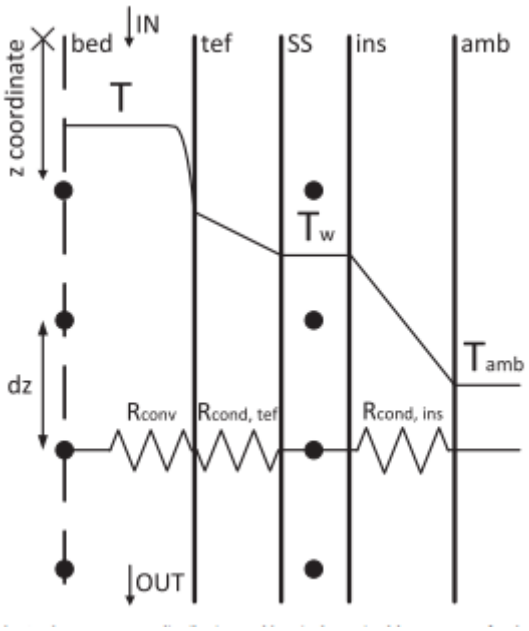

Figure 3.6: A scheme of the reactor model, with a bed temperature (T) and the wall temperature (T_w) connected by heat resistances in radial direction [14].

3.2.1.5 Theoretical Pressure Drop across the Reactor Bed

The pressure drop across the reactor bed is calculated from the Ergun equation (Equation 3.9) and is found to be 0.6 Pa. All the relevant values for calculation can be found in Appendix H. It must be noted that this pressure drop is calculated based on uniform air velocity, water vapor concentration at reactor inlet, uniform bed porosity and uniform distribution of particles.

$$\Delta P = \frac{150\,\mu_{air} L}{D^2}\,\frac{(1-\epsilon_b)^2}{\epsilon_b^3}u + \frac{1.75 L \rho_{air}}{D}\,\frac{(1-\epsilon_b)}{\epsilon_b^3}u|u| \qquad \text{Equation 3.9}$$

$$\Delta P = \left(\frac{150 \times 1.85 \times 10^{-5}\,\frac{kg}{m\cdot s} \times 0.12\,m}{(0.07\,m)^2} \times \frac{(1-0.54)^2}{0.54^3} \times 0.26\,\frac{m}{s}\right) + \left(\frac{1.75 \times 0.12\,m \times 1\,\frac{kg}{m^3}}{0.07\,m} \times \frac{(1-0.54)}{0.54^3} \times 0.26\,\frac{m}{s}\,|0.26|\frac{m}{s}\right) = 0.6\,Pa$$

3.2.2 Sample Preparation

A sample of 957 g of the K_2CO_3 composite is provided by the chemical company Caldic, in the Netherlands. It contains particles ranging up to 3 mm. To remove the particles <500 µm, sieving is done as shown in Figure 3.7. It is done to avoid any clogging that might have happened due to the presence of powder at the reactor bottom. Additionally, sieving allowed to understand the particle size distribution of the entire sample (957 g), which is performed with the available sieve sizes of 1 mm, 2 mm and 3.15 mm. Figure 3.8 shows the particle size distribution of the sample, with the majority of the particles equal to 2 mm. However, this is just an estimation because the grains are of irregular shapes. This would have been accurate if the grains were completely spherical. At the end of the sieving process, 423 g of the K_2CO_3 composite is added to the reactor.

Figure 3.7: Procedure of sieving performed to investigate the particle size distribution
[Left] Sieving with a sieve size of 500 µm to remove powder from the sample
[Middle] Sieving with a stack of sieve size of 1 mm, 2 mm and 3.15 mm
[Right] Total weight of the sample after sieving (including container weight)

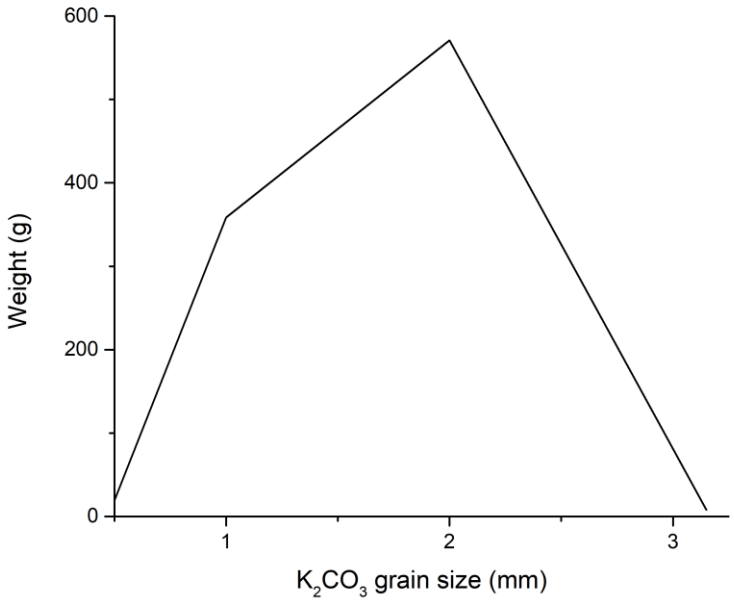

Figure 3.8: Particle size distribution of the entire sample (957 g) of K_2CO_3 composite, which indicates that the majority of the sample lies within the range of 2 mm.

3.2.3 Design of Experiments

Before analyzing the kinetic performance of K_2CO_3 composite, the experiments are designed, and the inlet variable parameters of the reactor setup are explained. There are three controlled parameters that can be varied.

- A mass flow rate of air at the reactor inlet, GFC
- Reactor inlet temperature, T_{in}
- Reactor inlet water vapor concentration, C_{in}

3.2.3.1 Design of Safety Conditions

Due to the risk of overhydration, low heat transport of K_2CO_3 and deliquescence at low temperatures [23], safety conditions are designed. To do so, certain conservative assumptions are taken. It is observed that the laboratory temperature varies between 22-24 °C. Hence, it is assumed that the K_2CO_3 composite will never attain temperatures below 21 °C in the reactor bed. From the phase diagram of K_2CO_3 (Figure 2.1), the water vapor pressure (p_{H_2O}) is 11 mbar at 21 °C. Therefore, the p_{H_2O} in the reactor should never be lower than 11 mbar. Otherwise, deliquescence can occur which may lead to material coagulation and irreversible changes in the material porosity [23]. Considering the worst-case scenario i.e. if the reactor bed attains 21 °C, then the maximum inlet water vapor concentration (C_{max}) will be 0.44 mol/m³ according to the relation $p_{H_2O} = C_{in}RT$. Thus, it is assumed that all the operating conditions must follow the condition of $C_{in} < C_{max}$. All the hydration experiments are performed while keeping the sample within the defined safety conditions.

For dehydration, the temperature range is selected i.e. $70\ °C \leq T_{dehydration} \leq 120\ °C$. There are a few reasons for selecting this temperature range. Firstly, in a typical thermochemical heat storage system application, solar collectors are used to absorbing the surplus amount of solar energy during summers to heat up the air. The typical operating temperatures for vacuum tube collectors range between 70 °C–120 °C [58]. Therefore, the realistic temperature range is considered for the dehydration, which is simulated by a heater in the reactor setup. Secondly, according to the thermodynamic selection criteria suitable for heat storage while considering domestic applications, the dehydration temperature should be <120 °C, as stated by Sogutoglu et. al. [59]. Lastly, to justify that the dehydration of K_2CO_3 composite occurs between 70-120 °C, an equilibrium temperature (T_{eq}) is calculated in Appendix A. From calculations, the p_{H_2O} is 7.7 mbar at 70 °C. From the phase diagram of K_2CO_3 (Figure 2.1), the T_{eq} is 52 °C at 7.7 mbar. This indicates that the experimental operating point i.e. 7.7 mbar at 70 °C, lies below the red line in the phase diagram of K_2CO_3 (Figure 2.1) and hence dehydration will occur.

3.2.3.2 Reference Scenario for Hydration & Dehydration

A reference scenario is developed for both hydration and dehydration as shown in Table 3.1. As mentioned earlier, the laboratory temperature varies between 22-24 °C. Therefore, to have a consistency in all the hydrations, the inlet air temperature (T_1) is taken as 25 °C. The CEM heater is used to attain 25 °C at reactor inlet. In the reactor setup, inlet water vapor concentration is controlled by the Liquid Flow Controller (LFC). Due to the technical limitations of the Bronkhorst® software, only two set-points of LFC i.e. 2 and 3% can be used, which corresponds to 0.3 mol/m³ and 0.4 mol/m³ respectively. With LFC higher than 0.4 mol/m³, the safety conditions are breached. Hence, between the two possibilities, 0.3 mol/m³ is considered for the reference scenario of hydration.

Table 3.1: Operating conditions of reference hydration & dehydration

	Mass Flow of Air (GFC)	Reactor Inlet Temperature (T_{in})	Inlet Water Vapor Concentration (C_{in})
	g/min	°C	mol/m³
Hydration	48	25	0.3
Dehydration	48	100	0.03

For the reference scenario of dehydration, 100 °C is taken as a dehydration temperature from 70-120 °C. It is selected so that the kinetic behavior of K_2CO_3 composite can be investigated above and below the reference temperature (100 °C). For the reference

scenario of both hydration and dehydration, the mass flow of air (GFC) is taken as 48 g/min, because the similar mass flow of air was used in this reactor setup in past research.

3.2.3.3 Preliminary Dehydration

At the start of the experimental phase, the state of K_2CO_3 composite i.e. either completely hydrated or dehydrated was unknown and may have contained CO_2. Therefore, initially, long dehydration is done by flushing the sample with 120 °C of hot air to remove H_2O and CO_2, which might be present in K_2CO_3. $KHCO_3$ formation usually occurs if K_2CO_3 is exposed to the CO_2 environment for a considerable amount of time [59]. After this long dehydration, it is assumed that the K_2CO_3 composite is completely dehydrated.

3.2.3.4 Experimental Phase

The experimental phase is classified into two main categories i.e. cyclic and planned experiments. The cyclic experiments are further divided into two phases with two different sets of operating conditions as mentioned in Table 3.2.

Table 3.2: Operating conditions of cyclic experiments (Phase 1 and 2)

	Mass Flow of Air (GFC)	Reactor Inlet Temperature (T_{in})	Inlet Water Vapor Concentration (C_{in})
	g/min	°C	mol/m³
Phase 1			
Hydration	48	25	0.3
Dehydration	48	100	0.03
Phase 2			
Hydration	48	25	0.4
Dehydration	48	120	0.03

Table 3.3: Operating conditions of planned experiments

Hydration				Dehydration			
Exp#	GFC	T_{in}	C_{in}	Exp#	GFC	T_{in}	C_{in}
	g/min	°C	mol/m³		g/min	°C	mol/m³
Ref Scenario	48	25	0.3	Ref Scenario	60	100	0.03
Case 0							
C0H1	48	25	0.4	-	-	-	
Case 1							
C1H1	60	25	0.3	C1D1	48	70	0.03
C1H2	54	25	0.3	C1D2	48	80	0.03
C1H3	42	25	0.3	C1D3	48	90	0.03
C1H4	36	25	0.3	C1D4	48	110	0.03
-	-	-	-	C1D5	48	120	0.03
Case 2							
C2H1	48	34	0.3	C2D1	60	100	0.03
C2H2	48	30	0.3	C2D2	54	100	0.03
C2H3	48	26	0.3	C2D3	42	100	0.03
C2H4	48	38	0.3	C2D4	36	100	0.03

In hydration, the inlet water vapor concentration is increased from 0.3 mol/m³ in phase 1 to 0.4 mol/m³ in phase 2. It is done to understand the kinetic performance of K_2CO_3 composite when the driving force is increased. In dehydration, the temperature is increased

from 100 °C in phase 1 to 120°C in phase 2. It is done to understand the kinetic performance of K_2CO_3 composite under two different dehydration temperatures. Also, it is known that the grid air has a relative humidity of 2.5%, which corresponds to 0.57 g(H_2O)/m^3(air) at reactor inlet and is taken during dehydration for precise measurements to calculate the amount of H_2O released.

The planned experiments are performed according to the experimental plan as mentioned in Table 3.3. The aim of these experiments is to understand the kinetic performance of K_2CO_3 composite under variable operating conditions. They are designed to change one parameter while keeping the other two parameters constant. For hydration, the parameters such as GFC and T_{in} are varied 4 times, whereas C_{in} is varied only once due to the limitation of the Bronkhorst® software. For dehydration, T_{in} and GFC are varied five and four times respectively.

3.2.3.5 Deliquescence check for Phase 1 & 2 hydration

Point 1 and 2 in Figure 3.9 represent inlet operating conditions of P1H1 (Phase 1 Hydration 1) and P2H6 (Phase 2 Hydration 6) experiments respectively. Phase 2 hydrations are closer to deliquescence line due to increased water vapor concentration at reactor inlet from 0.3 mol/m^3 to 0.4 mol/m^3, which implies that phase 2 reactions are possibly faster as compared to phase 1 reactions due to the increased driving force. The driving force is basically the pressure ratio between the water vapor (p_{H_2O}) and equilibrium pressure (P_{eq}) that drives the hydration reaction. Also, no deliquescence condition is reached in both phase 1 and 2 hydration experiments.

$$Driving\ Force = \frac{p_{H_2O}}{P_{eq}}$$

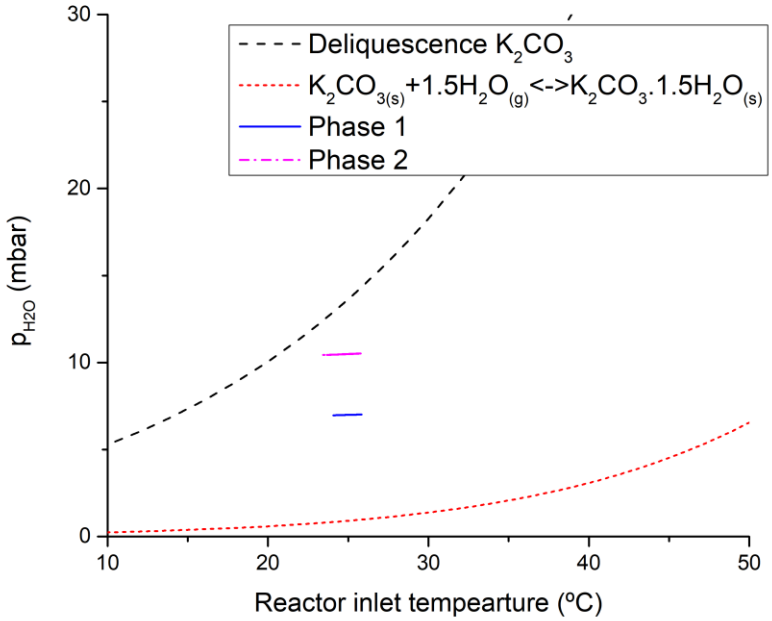

Figure 3.9: Point 1 and 2 represent the inlet operating conditions of P1H1 (Phase 1 Hydration 1) and P2H6 (Phase 2 Hydration 6) experiment respectively.

3.3 Reactor Energy Balance

The heat balance of the reactor is calculated by considering the energy flows as shown in Figure 3.10 and the equations used are mentioned in Table 3.4. When a mixture of air and water vapor enters the reactor, the energy is produced due to an exothermic reaction ($P_{reaction}$). This energy is calculated experimentally based on the mass flow rates of H_2O at the reactor inlet and outlet. This energy produced in the reactor, $P_{reaction}$ is consumed by three energy flows [14]:

- The amount of energy that leaves the reactor due to convective heat transfer by airflow across the reactor ($P_{convection}$). It is calculated as the difference between convective heat transfer of airflow at the reactor inlet $P_{air_{in}}$ and outlet $P_{air_{out}}$. Also, $P_{convection}$ is the amount of energy that is measured from the thermocouples at the inlet and outlet of the reactor.
- The amount of energy required to heat up the material by sensible heat transfer within the reactor ($P_{sensible}$). It is calculated based on the time derivative of the reactor bed temperatures i.e. (M1-M5) and thereby integrating them through the reactor length (L) to determine the experimental value.
- The amount of heat loss from the bed to the reactor body (P_{loss}). It is calculated based on ΔT between reactor inside and outside wall temperatures.

The heat balance across the reactor should be theoretically zero. In hydration, it is given by Equation 3.10, whereas in dehydration, it is given by Equation 3.11.

$$P_{convection} + P_{sensible} + P_{loss} = P_{reaction} \qquad \text{Equation 3.10}$$

$$P_{reaction} + P_{sensible} + P_{loss} = P_{convection} \qquad \text{Equation 3.11}$$

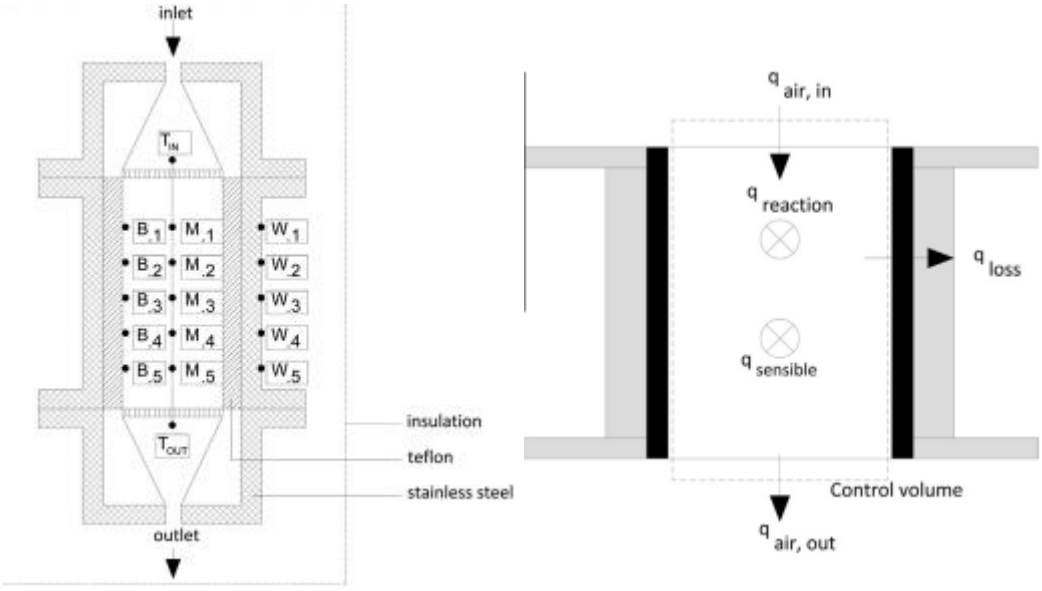

Figure 3.10: A schematic view of energy flows in the reactor [14]

Table 3.4: Reactor energy balance equations

#	Term	Experimental
1	$P_{convection}$	$P_{air_{out}} - P_{air_{in}}$
2	$P_{air_{in}}$	$\left(\dot{m}_a C_{p,a} + \dot{m}_{v,in}\, C_{p,v}\right) T_{in}$
3	$P_{air_{out}}$	$\left(\dot{m}_a C_{p,a} + \dot{m}_{v,out}\, C_{p,v}\right) T_{out}$
4	$P_{reaction}$	$\frac{\dot{m}_{v,in} - \dot{m}_{v,out}}{M_v} \Delta H$
5	$P_{sensible}$	$\sum_{i=1}^{5} \rho_{K_2CO_3} C_{p_{K_2CO_3}} A_i \frac{\Delta T_{Mi}}{\Delta t} \Delta L$
6	P_{loss}	$\sum_{i=1}^{5} (\frac{T_{Bi} - T_{Wi}}{R}) A_i$

Chapter 4 | Experimental results

This chapter includes the discussion of the possible formation of $KHCO_3$ during cyclic experiments, followed by the detailed analysis of preliminary dehydration. The reactor energy balance for reference hydration and preliminary dehydration is done. The results of cyclic experiments (phase 1 and 2) performed at two different sets of operating conditions are discussed to observe the cyclability of the K_2CO_3 composite. Also, the results of planned experiments are presented to provide an insight of the kinetic performance of K_2CO_3 composite by varying the inlet-controlled parameters.

4.1 $KHCO_3$ Formation

Numerous researches are done to investigate the ability of CO_2 absorption by K_2CO_3 under ambient conditions according to the reaction of Equation 4.1 and Equation 4.2 [60], [61], [59]. Sogutoglu et. al. [59] have superimposed the phase diagram of K_2CO_3 with the reactions of Equation 4.1 and Equation 4.2 on a graph (Figure 4.1). It is done to identify the boundary conditions of $KHCO_3$ formation, represented by the hatched region. The aim of this section is to find whether the experiments of this research project lies within the $KHCO_3$ region or not. Because $KHCO_3$ formation causes material degradation due to CO_2 interaction and consequent side reactions. In phase 1, K_2CO_3 composite is hydrated at p_{H_2O} = 7 mbar and 25 °C. Whereas in phase 2, K_2CO_3 composite is hydrated at p_{H_2O} = 10 mbar and 25 °C. In Figure 4.1, the yellow circle and blue square point represent the conditions of phase 1 and 2 respectively. This indicates that the cyclic experiments (hydration) are within the region of $KHCO_3$ formation and there is a possibility that during cyclic experiments (hydration), part of the energy is consumed in side reactions (as mentioned by Equation 4.1).

$$K_2CO_{3(s)} + H_2O_{(g)} + CO_{2(g)} \rightleftharpoons 2\,KHCO_3 \qquad \text{Equation 4.1}$$

$$K_2CO_3 \cdot 1.5H_2O_{(s)} + CO_{2(g)} \rightleftharpoons 2\,KHCO_3 + 0.5\,H_2O_{(g)} \qquad \text{Equation 4.2}$$

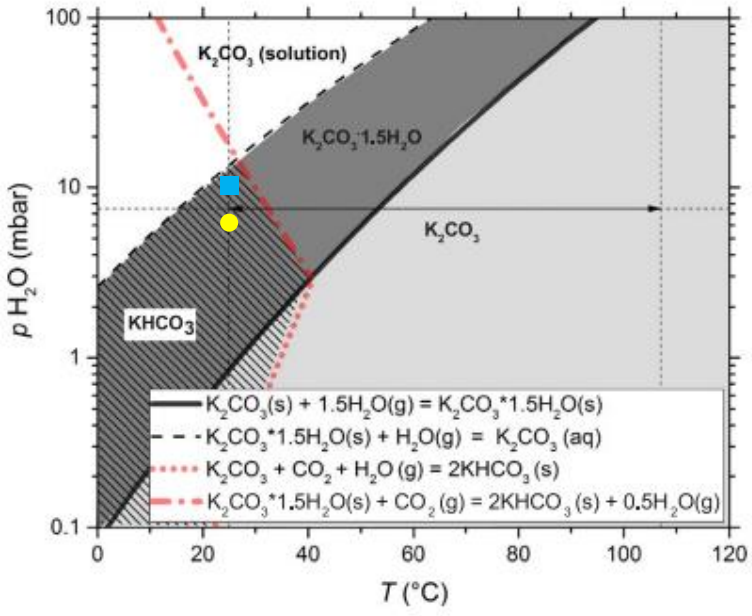

Figure 4.1: Phase diagram for reactions Equation 4.1 and Equation 4.2 at p_{H_2O} = 0.4 mbar [59]. The hatched region shows $KHCO_3$ formation conditions. Yellow circle and blue square point show operating conditions of phase 1 and 2 hydrations respectively.

4.2 Results of Preliminary Dehydration

Before cyclic experiments, long dehydration (Figure 4.2) is performed at 120 °C for nearly 17 h. This is done because at the beginning of the experimental phase, the state of the K_2CO_3 composite was unknown i.e. either hydrated or dehydrated. Therefore, long dehydration is done to make sure that all the H_2O absorbed in the K_2CO_3 composite is removed, and also to get rid of any CO_2, which might be present in the given sample according to Equation 4.1.

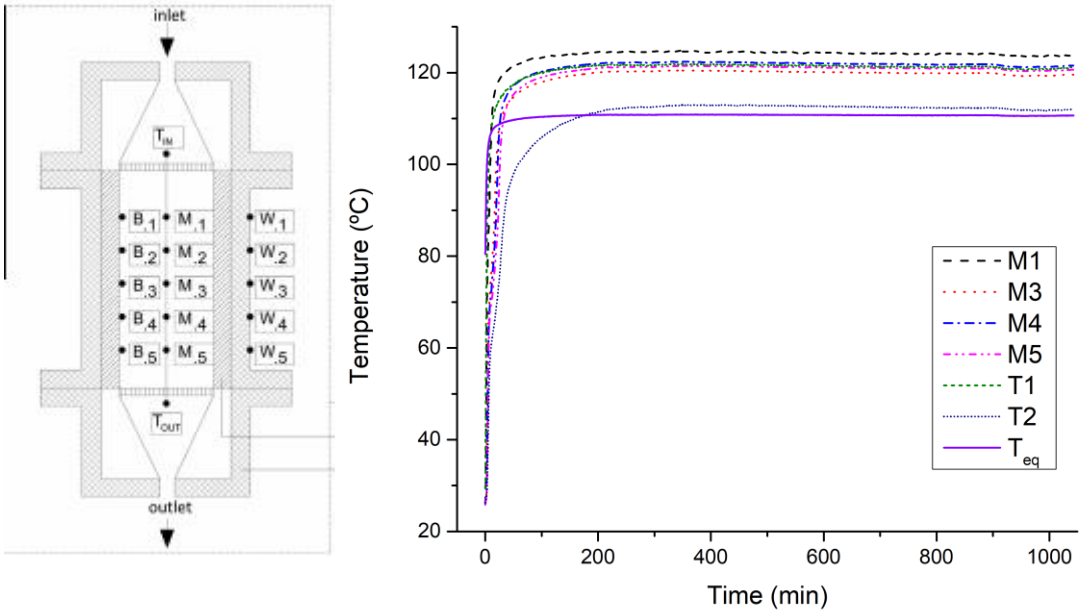

Figure 4.2: Preliminary dehydration with the inlet air temperature at 120 °C for 17 h to get rid of H_2O and possibly entrapped CO_2 in the material.

Figure 4.2 shows that all the reactor bed temperatures (M1–M5) reached the reactor inlet temperature T1, which is one of the indication that the dehydration reaction is finished. It can also be seen that M1 > T1. Conversely, M1 should be less than T1 because T1 is placed before M1 and is the first thermocouple that is in contact with the hot air. The temperature difference is 2.8 °C at the end of the experiment between M1 and T1. In the reactor setup, T-type thermocouples are used for the bed temperatures (M1–M5) and T1. Generally, T-type thermocouples have the error level of ±1 °C [62]. Therefore, ΔT=2.8 °C is possibly due to the accuracy error of thermocouples and miss-calibration. Also, the difference between the mass flow rate of H_2O at reactor inlet and outlet (Figure 4.3) is possibly due to the inaccuracy of humidity sensor because the working range of the sensor is between -40 °C to 80 °C. Whereas the outlet temperature is above 80 °C. All the bed temperatures from M1–M5 are above T_{eq} line, which justifies that K_2CO_3 composite is effectively completely dehydrated. Also, for further dehydration, the same assumption is taken if the tail of dehydration curve is horizontal (Figure 4.3), then the dehydration reaction is finished.

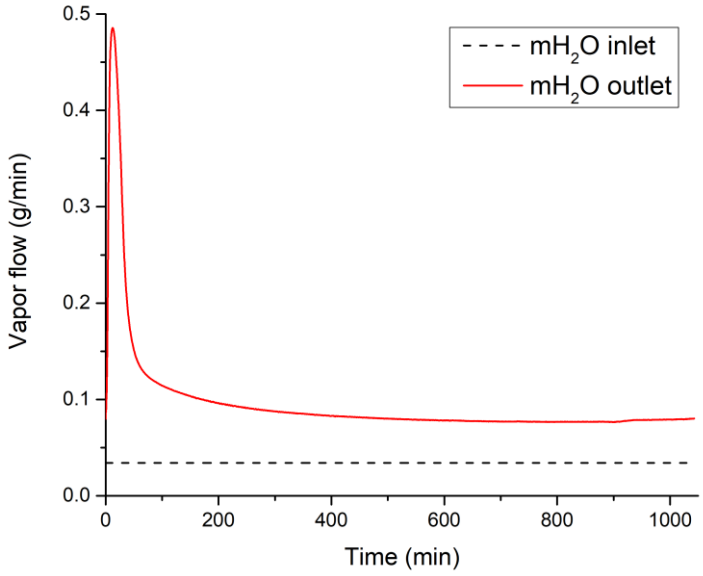

Figure 4.3: Vapour flow at the reactor inlet & outlet in preliminary dehydration. At the inlet, RH of grid air is 2.5%, which corresponds to 0.03 g/min of H_2O flow.

Figure 4.4 shows the temperature profile of the reactor from center to the outside wall for 2 different reactor bed positions during dehydration. These positions are bed 1 (reactor top) and bed 5 (reactor bottom). Blue and green color represent bed 1 and 5 position respectively in Figure 4.4. The ΔT=M1-B1=22 °C, which implies that there is a notable temperature difference at the same bed height within the reactor from center to the inside wall. Also, ΔT=M5–B5=31 °C, which is higher than the bed 1 position. From this, the following hypothesis could be deduced:

- Firstly, the hot air is in contact first with the bed position 1, thereby transferring sensible heat to grains of K_2CO_3 composite and inside the reactor wall. As the hot air moves down, the temperature decreases due to the possible hindrance caused by the thermal mass. Hence, B5 is lower in temperature than B1.
- Secondly, the temperature is not uniformly distributed across the same bed height i.e. the temperature at the middle of the reactor bed 1 is higher (M1=120 °C) than at the inside reactor wall (B1=102 °C) at the end of the experiment.

To understand the temperature flow across the reactor wall, the difference between inside and outside wall temperature at bed position 1 and 5 is shown in Figure 4.5. The ΔT is higher across the reactor wall at the top than at the bottom. This is because of B1 > B5 due to the possible reason mentioned above.

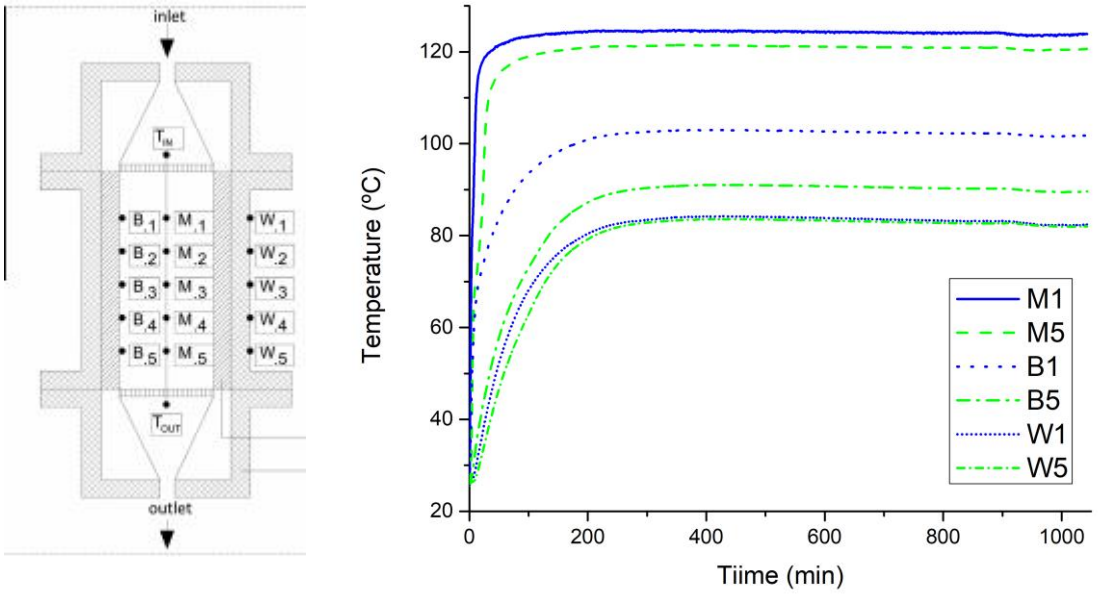

Figure 4.4: Temperature profile of the reactor for bed position 1 (blue) and 5 (green) during dehydration of K_2CO_3 composite.

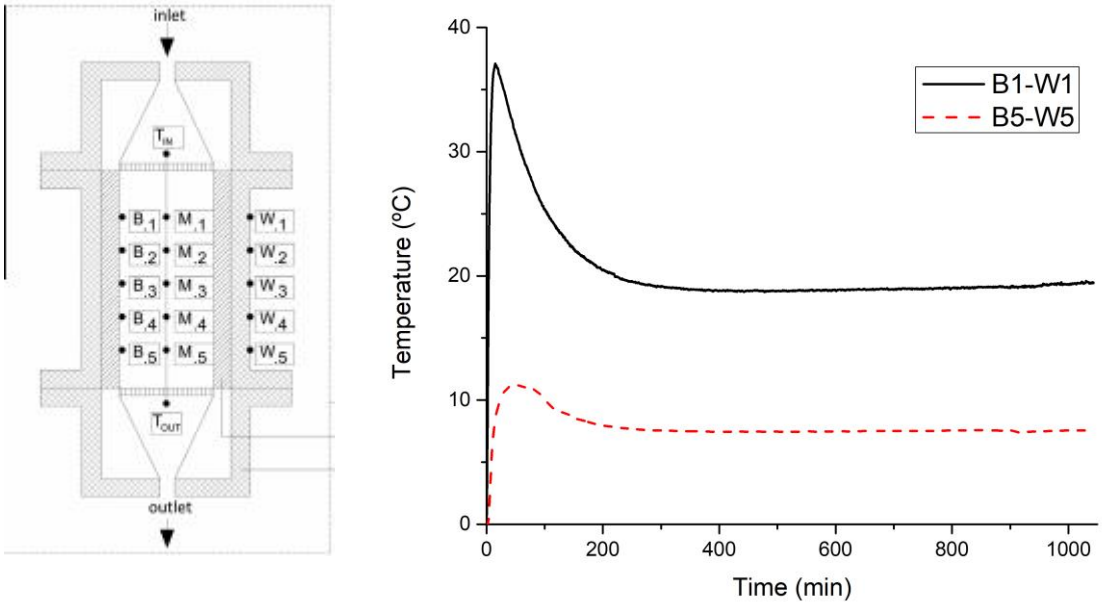

Figure 4.5: Temperature difference between reactor inside (B) and outside wall (W) for bed position 1 and 5 during dehydration of K_2CO_3 composite

4.3 Results of Reactor Energy Balance

4.3.1 Preliminary Dehydration

The heat balance is calculated for preliminary dehydration performed at 120 °C with the airflow rate of 48 g/min and the resulting energies are presented in Table 4.1. In dehydration, $E_{convection}$ is negative, which implies that $E_{out} < E_{in}$. This is because K_2CO_3 composite in the reactor is absorbing energy during dehydration. Also, $P_{convection}$ is the

largest term because it has to provide the power for $P_{reaction}$, $P_{sensible}$ and P_{loss} according to the energy balance (Equation 3.11). Figure 4.6 shows that $P_{reaction}$ increases in the beginning and then decreases. The P_{loss} is higher in the beginning and gradually decreases. This may be due to the high-temperature difference between inside and outside the reactor wall at the beginning. Also, initially, the reactor bed is at room temperature. As the hot air enters the reactor inlet, the heat transfer to the wall also increases, until it attains a constant temperature. This P_{loss} is also much higher in comparison with hydration because the higher amount of heat is possibly needed to heat up the inside wall. The P_{loss} are driven by the temperature difference between the inside and outside the reactor wall. Figure 4.7 shows that $P_{sensible}$ also increases, in the beginning, to heat up the material and reactor body. Once the material attains a constant temperature, sensible heat transfer diminishes. The error is may be due to the RH sensor because the working range of sensor probes is between -40 °C to 80 °C, whereas the operating temperature is higher. Also, the amount of sensible heat required to heat up the filter and other components is not taken into consideration, which could be one of the possible reasons for error.

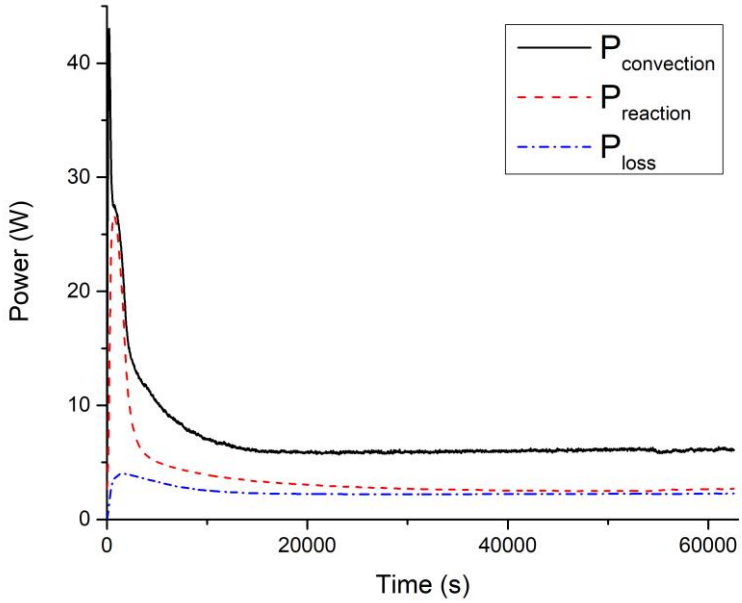

Figure 4.6: Heat fluxes in the reactor during the preliminary dehydration at 120 °C

Table 4.1: Total energies for the reactor energy balance of reference hydration and preliminary dehydration

Term	Reference Hydration	Preliminary Dehydration
	kJ	kJ
$E_{convection}$	67	-449
$E_{reaction}$	86	227
$E_{sensible}$	10	82
E_{loss}	1	150
Error	-8	10

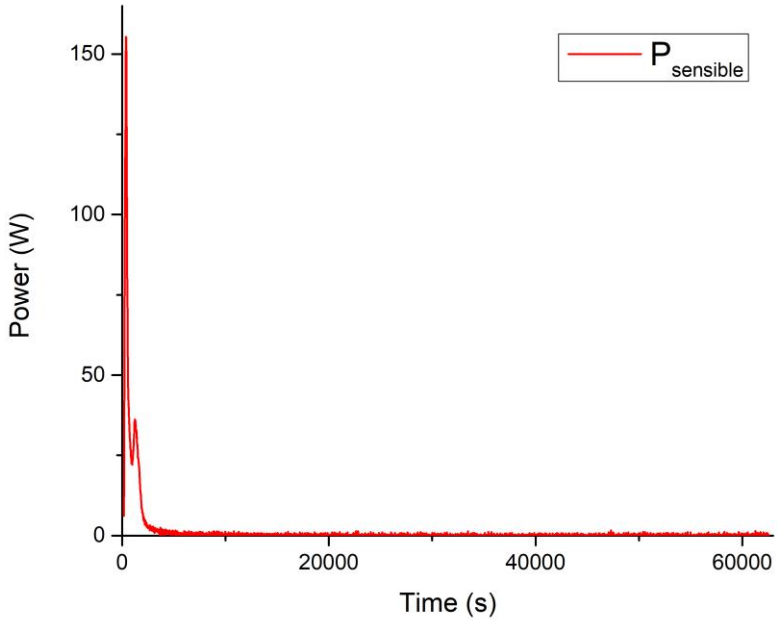

Figure 4.7: Sensible heat loss in the reactor during the preliminary dehydration at 120 °C

4.3.2 Reference Hydration

The heat balance is calculated for a reference hydration performed according to the operating conditions mentioned in Table 3.1 and the resulting energies are presented in Table 4.1. Figure 4.8 shows that $P_{reaction}$ increases in the beginning and then decreases gradually. This decrease and slow passing of the reaction from the top to the bottom of the reactor (thermal front) may be due to the slow kinetics of K_2CO_3 composite. Also, the sudden peak of $P_{reaction}$, in the beginning, is possibly due to the faster completion of reaction at the bed regions adjacent to the wall, whereas the middle bed region continues to absorb vapor. Few possible reasons of this effect could be incomplete drying of K_2CO_3 composite grains near wall regions due to heat losses to the wall, or due to higher porosity near the wall allowing an easier path for water vapor diffusion. The later may be considered true, as also observed visually, when the reactor was opened at the end of hydration. It was seen that the grains are less accumulated near wall region than at the center, allowing enhanced bed porosity at the region near the wall. $P_{convection}$ also follows the similar trend as $P_{reaction}$. As the energy produced due to H_2O absorption is higher in the beginning, E_{out} is also higher, thereby giving a high peak of $P_{convection}$ in the beginning. P_{loss} and $P_{sensible}$ are negligible as compared to reaction heat and the convection heat transfer by the airflow. Figure 4.9 shows that $P_{sensible}$ is much higher in the beginning. This may be explained that the grains of the K_2CO_3 composite are at the room temperature in the beginning and as soon as the reaction occurs, part of the energy is consumed to heat up the material. After 7 min, the $P_{sensible}$ becomes negative. It means that the material possibly releases part of its sensible heat back to the bed. The heat loss through the wall, P_{loss} is higher in the beginning because of the high energy released due to the reaction in the beginning. This caused an increase in the inside wall temperature and hence the ΔT between inside and outside wall is higher in the beginning and later both the walls attained a similar temperature. The error might be due to other heat transfer such as sensible heat transfer to Teflon wall and filter at the reactor bottom, which are not taken into consideration.

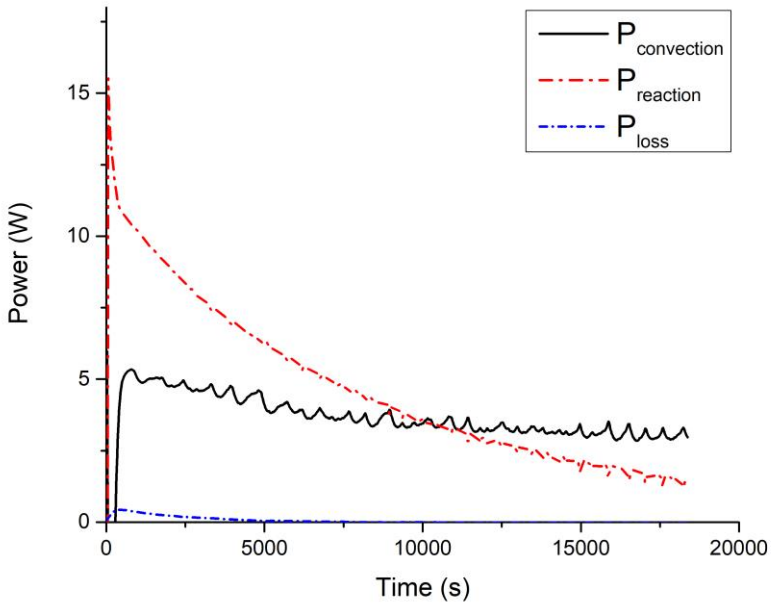

Figure 4.8: Heat fluxes in the reactor during the reference hydration

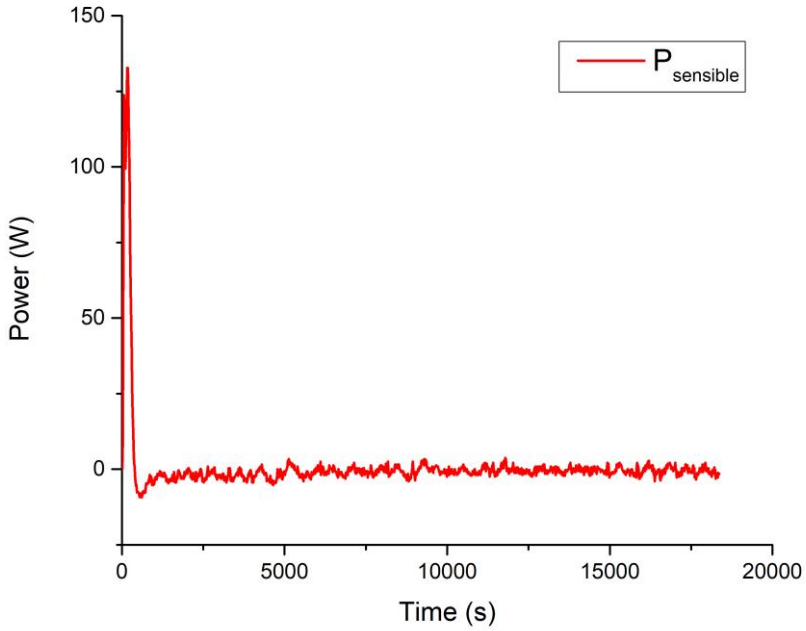

Figure 4.9: Sensible heat loss in the reactor during the reference hydration

4.4 Results of Cyclic Experiments

4.4.1 Phase 1

In phase 1, 9 experiments are performed in total i.e. 5 hydration and 4 dehydration, under the operating conditions as mentioned in Table 3.1, to realize the cyclability of the K_2CO_3 composite. Dehydration P1D0 (Phase 1 Dehydration 0) is the preliminary experiment performed to remove H_2O and CO_2 as mentioned earlier, to determine the state of the K_2CO_3 composite. It is assumed to be completely dehydrated after this experiment. The experiments are performed for different time durations and the lengths of original time are shown in Appendix E. To develop a common ground for comparison, all the experiments are reduced to equal time periods i.e. 5 h 6 min of P1H2 (Phase 1 Hydration 2) as shown in Table 4.2. The experiments P1D4 and P1H5 are not considered for comparison and criteria for reducing experiments. The data for P1D4 and P1H5 are logged only for 3 h 24 min because the Pico-log software got hanged and the retrieval of full data for these experiments was not possible. P1H2 is chosen as a criterion for reducing experiments because it is the second least time duration of phase 1 experiments after P1D4 and P1H5. Also, it can be seen from Figure 4.11 that after 5 h 6 min, the dehydration curves are horizontal at the end, which indicates that the reaction is finished. Figure 4.10 indicates that the mass flow rate of water (m_{H_2O}) at the inlet is nearly equal to the outlet, which indicates that the hydration is nearly finished. If m_{H_2O} at the reactor inlet becomes equal to the outlet, it means that the reactor bed is fully hydrated, and no more water can be absorbed by the material. Hence, 5 h 6 min is a conservative assumption that the majority of the reaction is finished within this time.

Table 4.2: Results of cyclic experiments (Phase 1). P1D0, P1D4 and P1H5 are not considered for comparison. Green and orange color show hydration and dehydration.

Exp#	Experiment	Water Absorbed/ Released (g)	$E_{convection}$ (kJ)	Peak Discharge Temp. (°C)	Time (min)
PID0	Dehydration	64	-449	-	17 h 23 min
P1H1	Hydration	24	67	36	5 h 6 min
P1D1	Dehydration	58	-199	-	5 h 6 min
P1H2	Hydration	14	50	31	5 h 6 min
P1D2	Dehydration	47	-195	-	5 h 6 min
P1H3	Hydration	17	43	32	5 h 6 min
P1D4	Dehydration	34	-202	-	5 h 6 min
P1H4	Hydration	19	42	33	5 h 6 min
P1D4	Dehydration	22	-160	-	3 h 24 min
P1H5	Hydration	15	27	31	3 h 24 min

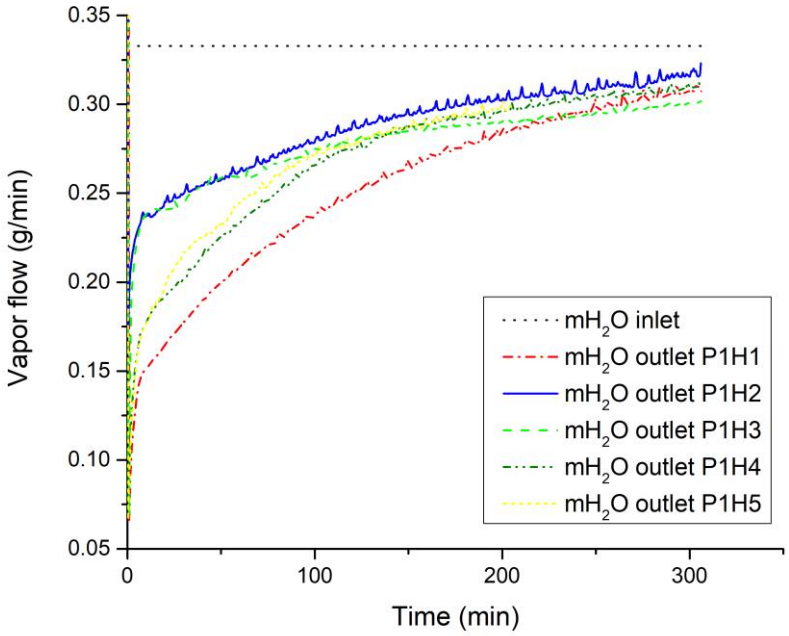

Figure 4.10: Vapor flow at reactor inlet & outlet for phase 1 hydration reactions

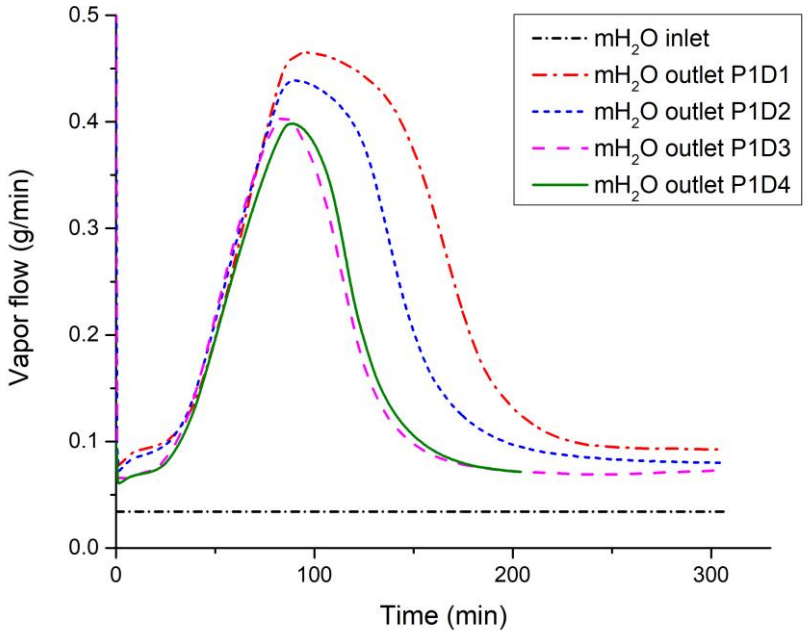

Figure 4.11: Vapor flow at reactor inlet & outlet for phase 1 dehydration reactions

Table 4.2 shows the amount of H_2O and energy absorbed/released during the alternative dehydration/hydration reactions. In P1H1, the K_2CO_3 composite absorbed 24 g of H_2O. The hydration is not completely finished, as seen in Figure 4.10 that the m_{H_2O} at the outlet is not equal to the inlet. One of the hypotheses for incomplete hydration even after 5 h 6 min is due to low driving force, which is not sufficient to release effectively the stored heat in the

K_2CO_3 composite. Secondly, at the beginning of the reaction, kinetics of the material is possibly slow. In P1H1, the energy obtained at the end of hydration reaction is 67 kJ. In P1D1, the K_2CO_3 composite released 58 g of H_2O, which is 34 g more than absorbed in P1H1 in 5 h 6 min. Also, in P1D2, 47 g of H_2O is released, which is 33 g more than absorbed in previous hydration (P1H2) in 5 h 6 min. It must be noted that the experiments are reduced to 5 h 6 min. The material will possibly continue to absorb water after 5 h 6 min during hydration. But probably due to the slow kinetics of the material, the material takes up only a small amount of water in 5 h 6 min. Conversely, during dehydration, the material is releasing more water in 5 h 6 min. In P1D1, 199 kJ of energy is provided by air during dehydration reaction. However, only 50 kJ of energy is obtained in the next hydration (P1H2). The reduction in energy content, H_2O absorption capacity and peak discharge temperature of the K_2CO_3 composite in consecutive hydration and dehydration cycles may be explained by the slow material kinetics under similar operating conditions, as explained by Ferchaud et. al. [27] as well while investigating $MgSO_4$ salt hydrate. Also, it is possible that part of the energy may be consumed in side-reactions with CO_2 to form $KHCO_3$ (as shown by Equation 4.1). The peak discharge temperature during phase 1 hydrations varies between 31 °C–36 °C, which is sufficient for domestic space heating applications.

It must be noted that the experiments are performed once per day and after finishing the experiment, the reactor is left for overnight to attain ambient temperature with both inlet and outlet reactor valves closed. But because the reactor is not completely airtight, there is a possibility of airflow from ambient to the reactor. Due to this, the material possibly absorbed some portion of the water present in the air due to its hygroscopic nature during overnight cooling. To investigate this hypothesis, two tests are performed.

Test 1: Reactor Leakage

It is checked whether the reactor is airtight or has some leakages. To do that, the reactor outlet valve is closed and is pressurized by flowing the air at 7 bars from GFC controller. The pressure inside the reactor is measured by the pressure gauge attached to the reactor. After attaining a pressure of 3 bar in the reactor, the inlet valve is closed. It is seen that the pressure started to fall and finally became zero. This proves that the reactor is not completely airtight and there are leakages.

Test 2: Water absorption during overnight cooling of the sample

It is checked whether the K_2CO_3 composite absorbs water if it is left open in the laboratory under ambient conditions for overnight cooling. To do that, a 200 g of the K_2CO_3 composite is taken and then placed in a convection heater for 24 h at 100 °C (Figure 4.12). Before placing the sample in the convection heater, the state of the sample was not known i.e. either hydrated or dehydrated. After 24 h, the sample is completely dehydrated, and it weighed 194 g (after excluding the beaker weight of 173 g), which indicates that the material lost 6 g of H_2O during dehydration. This dehydrated sample is left in the laboratory ambient condition for 24 h to see whether the material absorbs moisture from the ambient air or not. After 24 h, the sample weighted 199 g (after excluding the beaker weight of 173 g) and absorbed 5 g of H_2O. This shows that the K_2CO_3 composite in the reactor possibly also absorbed some portion of the water from the ambient air through reactor leakage during the overnight cooling. However, it is just a hypothesis and no calculations are done for quantifying the amount of water absorbed by the material in the reactor during overnight cooling.

Figure 4.12:[Top Left] 200 g sample after taring the weight of the beaker
[Top Right] The sample is placed in the convection heater for 24 h at 100 °C
[Bottom Left] The weight of the dehydrated sample + beaker (173 g) is 367 g
[Bottom Right] After 24 h, the weight of sample + beaker (173 g) is 372 g. This shows that during overnight cooling, the sample absorbed 5 g of H_2O.

4.4.1.1 Reactor Opening at the end of phase 1 cyclic experiments

At the end of phase 1 experiments, the reactor was opened twice: after hydration and after dehydration, to visually analyze the grains of the K_2CO_3 composite. After hydration, the grains are darker (Figure 4.13 and Figure 4.14) due to absorbed H_2O, relatively fragile and turns into powder if a small amount of force is applied. After dehydration, the grains are lighter in color due to the absence of H_2O and a small amount of force is required to move the grains in the bed. Also, it is observed that the grains are more accumulated at the center of the reactor rather than at the regions near the wall. This implies that the porosity is higher in the region near the wall as compared to the center.

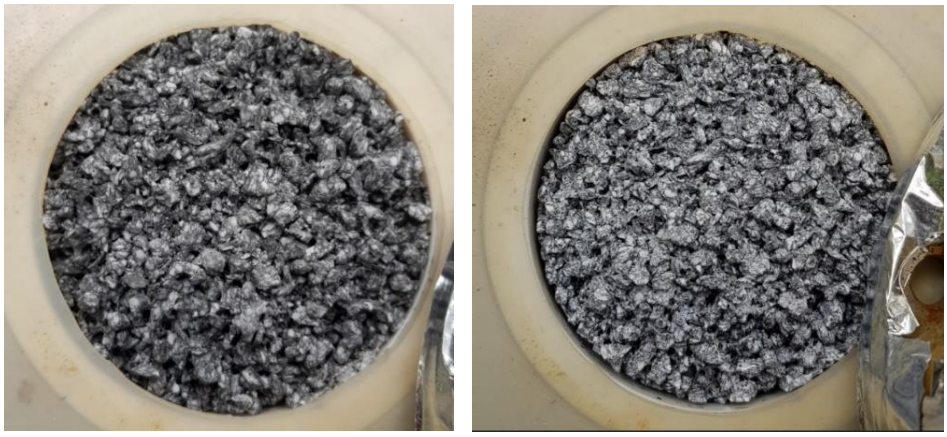

Figure 4.13: Reactor opened to investigate the physical appearance of the K_2CO_3 composite at the end of phase 1 cyclic experiments. Hydration (Left, Darker), Dehydration (Right, Lighter)

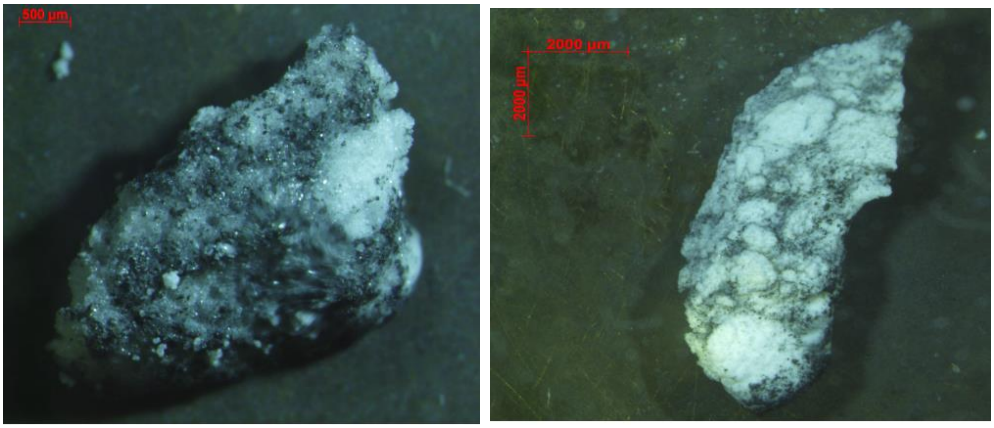

Figure 4.14: Microscopic picture of a single grain of K_2CO_3 composite. Hydration (Left, Darker), Dehydration (Right, Lighter)

4.4.2 Phase 2

In phase 2, 9 experiments are performed in total i.e. 5 dehydration and 4 hydration. Table 4.3 shows the results obtained from phase 2 experiments, performed according to the operating conditions mentioned in Table 3.1. Figure 4.15 and Figure 4.16 show the outlet mass flow of H_2O absorbed and released during phase 2 experiments respectively. Like phase 1, phase 2 experiments are also performed for different time durations and thereby reduced to equal time periods of 5 h 6 min, to develop consistency among phase 1 and 2 experiments for the sake of comparison. The lengths of original time of phase 2 experiments are shown in Appendix E. It is assumed that the hydration is nearly finished, whereas the dehydration is finished due to the horizontal curves at the end of the experiments. P2D1 is not considered for comparison. The data for P2D1 is logged only for 3 h 30 min because after that the Pico-log software got hanged and the retrieval of full data for the experiment was not possible.

Table 4.3: Results of cyclic experiments (Phase 2). P2D1 is not considered for comparison. Green and orange color show alternative hydration and dehydration respectively.

Exp#	Experiment	Water Absorbed/ Released (g)	$E_{convection}$ (kJ)	Peak Discharge Temp. (°C)	Time (min)
P2D1	Dehydration	26	-197	-	3 h 30 min
P2H1	Hydration	38	66	39	5 h 6 min
P2D2	Dehydration	57	-287	-	5 h 6 min
P2H2	Hydration	48	72	38	5 h 6 min
P2D3	Dehydration	67	-269	-	5 h 6 min
P2H3	Hydration	47	77	36	5 h 6 min
P2D4	Dehydration	65	-279	-	5 h 6 min
P2H4	Hydration	48	69	36	5 h 6 min
P2D5	Dehydration	55	-307	-	5 h 6 min

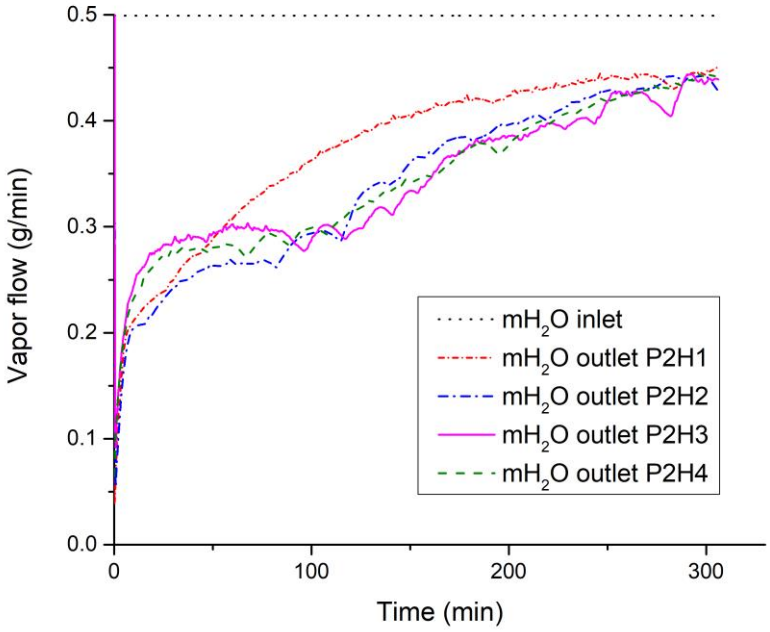

Figure 4.15: Vapor flow at reactor inlet & outlet for phase 2 hydration reactions

Phase 2 starts with dehydration reaction (P2D1) because the last experiment performed in phase 1 is hydration reaction (P1H5). In P2D1, the H_2O released is only 26 g because P1H5 absorbed only 15 g of H_2O, as can be seen in Table 4.2. Again, the water released in dehydration is more than absorbed in previous hydration because of the same reason as explained in phase 1. That is, the material possibly has slower kinetics during hydration due to which it absorbs less water in 5 h 6 min. It possibly continues to absorb more after 5 h 6 min. In P2H1, the material absorbed 38 g of H_2O, which is roughly twice the amount of H_2O absorbed in phase 1 hydrations. One of the possible reasons is increased driving force (by increasing inlet water vapor concentration from 0.3 mol/m^3 to 0.4 mol/m^3). Secondly, the water vapor transport may be increased due to the development of cracks and the opening of pores by consecutive contraction and expansion of the lattice structure over cycles, as also seen by Ferchaud [27] during grain level investigation of $MgCl_2.6H_2O$. In P2H2, P2H3

and P2H4, the material absorbed on average 48 g of H_2O i.e. replicating similar results consecutively within the duration of 5 h 6 min. Based on this, it may be concluded that the material has attained cyclability. The peak discharge temperature during phase 2 hydrations varies between 36 °C–39 °C, which is higher than phase 1 and is sufficient for domestic space heating applications.

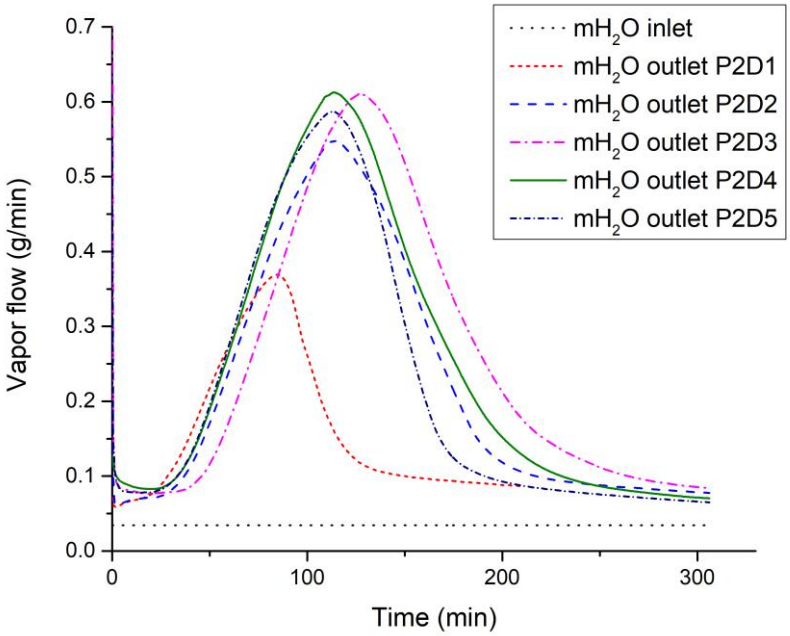

Figure 4.16: Vapor flow at reactor inlet & outlet for phase 2 dehydration reactions

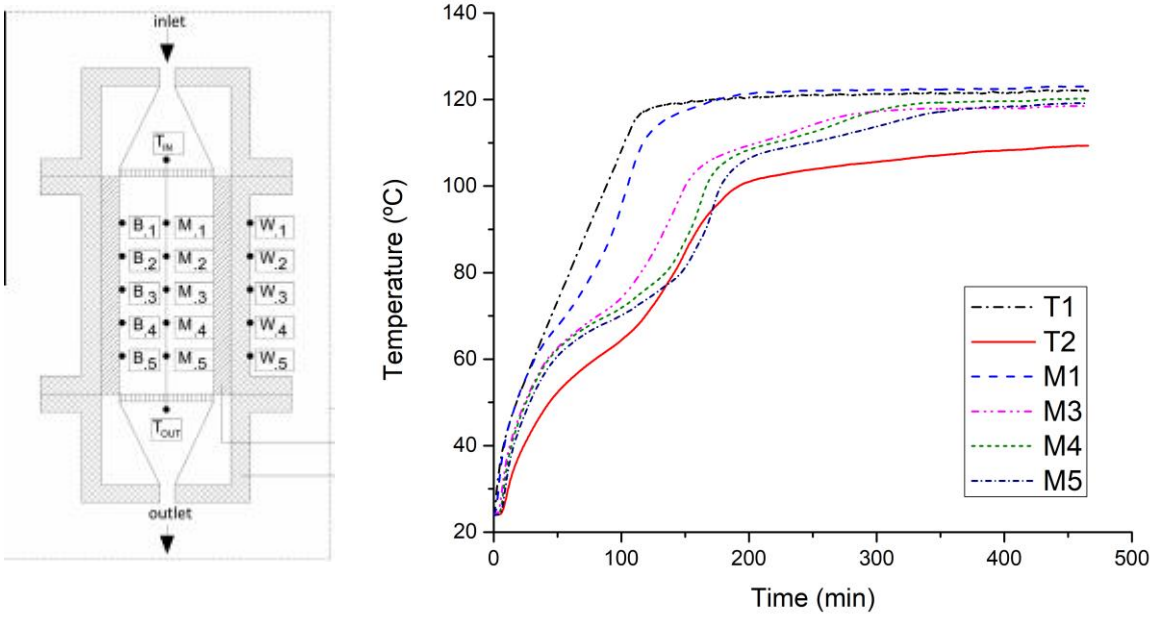

Figure 4.17: Formation of cold zones at reactor bottom due to which hot air is bypassed and hence T2 > M5. It is also seen when the reactor was opened after experimentations.

4.4.2.1 Formation of Dead Zones

In phase 2, the last three dehydrations (P2D2, P2D3, P2D4) reveal that the reactor outlet temperature (T2) is higher than the lowest bed temperature (M5). Conversely, T2 should be lower than M5 because it is placed outside the reactor. P2D2 is shown in Figure 4.17, while the graphs of P2D3 and P2D4 can be found in the Appendix F. This illustrates that some dead zones are formed at the reactor bottom, which is also seen when the bottom of the reactor is opened at the end of the experimental phase (see below section 4.5.3). Due to the formation of dead zones, the hot air is bypassed causing T2 > M5.

4.5 Results of Planned Experiments

Planned experiments are performed by varying one inlet-controlled parameter while keeping the other two as constant. The aim is to find out the kinetic performance of K_2CO_3 composite under variable operating conditions at reactor-scale. This section provides discussion of results performed according to the experimental plan as mentioned in Table 3.3, and analysis of the final outcomes.

4.5.1 Hydration

As concluded from the cyclic experiments that K_2CO_3 composite has attained a cyclic nature, the material is then used to perform experiments. The planned experiments are done with alternative hydration and dehydration. In Table 4.4, green and orange color represents hydration and dehydration respectively and the results are presented in the order of experiments originally performed in one table for the ease of understanding. The hydrations are stopped when the amount of water flow at the outlet becomes nearly equal to the water flow at the inlet. At the beginning, reference hydration and dehydration are performed to analyze the difference in kinetic performance of K_2CO_3 composite when the material is exposed to variable operating conditions.

Case 0: Variable C_{in} and Constant T_{in} & GFC

By increasing the inlet water vapor concentration (C_{in}) from 0.3 mol/m^3 (reference scenario) to 0.4 mol/m^3 in C0H1, it is observed that the material absorbed more H_2O (51 g) as compared to reference scenario (38 g). This effect is possibly due to the increased driving force, which allows the material to absorb more H_2O. Also, in C0H1, the heat obtained at the end of hydration reaction is 181 kJ, which is higher than reference scenario (133 kJ). This implies that the amount of H_2O absorbed during hydration is directly proportional to amount of heat obtained at the end of hydration. The peak discharge temperature is 38 °C, which is sufficient for domestic space heating applications.

Case 1: Variable GFC and Constant T_{in} & C_{in}

By decreasing the mass flow rate at the reactor inlet (GFC) during hydration, the amount of H_2O absorbed is increased. One of the possible reason could be that with lower mass flow rate of air, the mixture of air and water vapor leaving the CEM has more residence time to react with K_2CO_3 composite, and therefore more H_2O is absorbed and vice versa. With GFC of 60 g/min, the material absorbed only 18 g of H_2O, whereas with GFC of 36 g/min, the material absorbed 55 g of H_2O. Figure 4.18 shows that C1H4 has slow rate of H_2O released at reactor outlet as compared to C1H1-C1H3. Also, it shows that with high mass flow rate of air, the reaction is finished quickly. It must be noted that intermediate dehydrations are done at different temperatures, which might have changed the behavior of water absorption of material in following hydrations. The peak discharge temperature varies between 28 °C–39 °C, which is sufficient for domestic space heating applications.

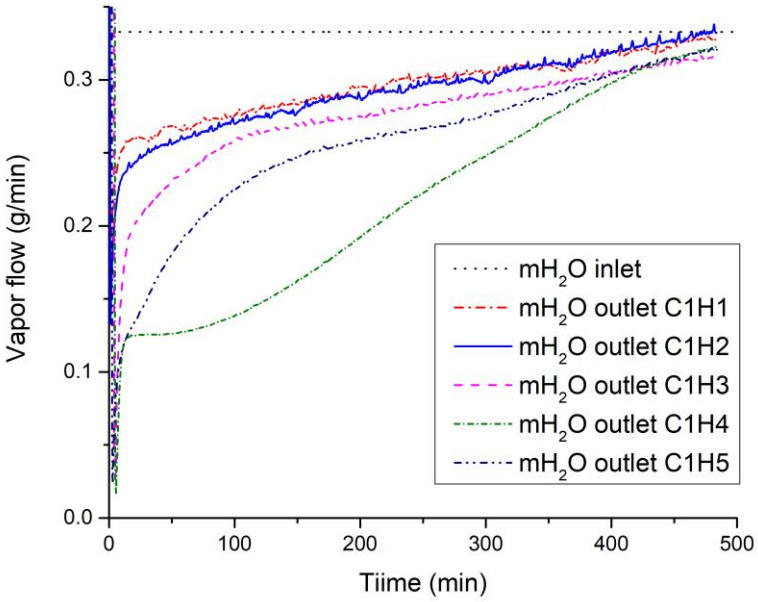

Figure 4.18: Vapor flow at reactor inlet & outlet for case 1 hydrations performed according to the operating conditions mentioned in Table 3.3.

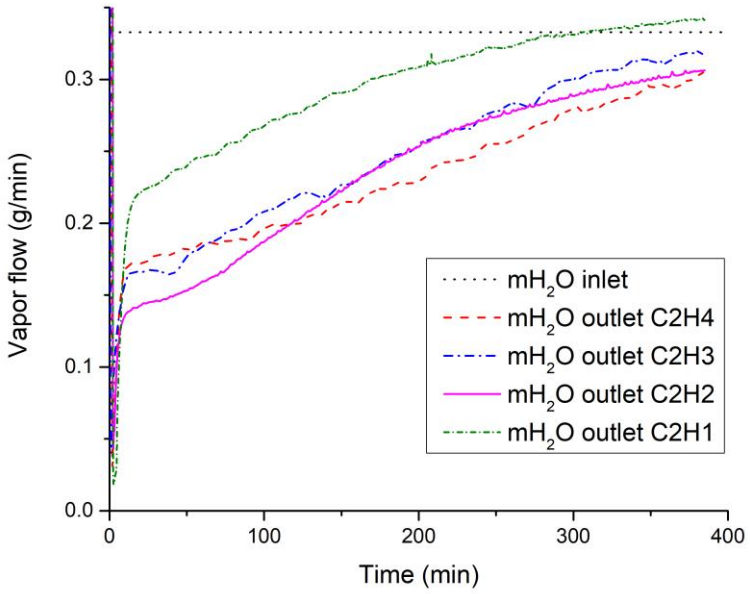

Figure 4.19: Vapor flow at reactor inlet & outlet for case 2 hydrations performed according to the operating conditions mentioned in Table 3.3.

Case 2: Variable T_{in} and Constant GFC & C_{in}

By decreasing the reactor inlet temperature (T_{in}) from 34 °C–26 °C, the amount of H_2O absorbed decreased by only 2 g i.e. from 39 g to 37 g. But when the reactor inlet temperature is raised to 38 °C, the material absorbed only 15 g of H_2O. Figure 4.19 shows that C2H4 finished quickly and the mass flow of H_2O at outlet exceeds that of inlet. This indicates that because of high inlet temperature, the K_2CO_3 composite is also releasing the water absorbed by the material due to which energy obtained at the end of the reaction is extremely low i.e.

-7 kJ. The peak discharge temperature varies between 35 °C–41 °C, which is sufficient for domestic space heating applications.

Table 4.4: Results of planned experiments performed under operating conditions as mentioned in Table 3.3 and are presented in the order of experiments originally performed. Green and orange color represents hydration and dehydration respectively.

Exp#	GFC	T_{in}	C_{in}	H_2O absorbed/released	$E_{convection}$	Peak Discharge Temp.	Time
	g/min	°C	mol/m³	g	kJ	°C	min
Ref	48	25	0.3	38	75	34	7h 12min
Ref	48	100	-	54	-380	-	9h 15min
Case 0							
C0H1	48	25	0.4	51	107	38	9h 15min
Case 1							
C1D1	48	70	-	20	-193	-	7h 7min
C1H1	60	25	0.3	18	59	28	8h 4min
C1D2	48	80	-	47	-242	-	7h 7min
C1H2	54	25	0.3	20	63	29	8h 4min
C1D3	48	90	-	40	-278	-	7h 7min
C1H3	42	25	0.3	41	56	33	8h 4min
C1D4	48	110	-	48	-384	-	7h 7min
C1H4	36	25	0.3	55	99	39	8h 4min
C1D5	48	120	-	65	-431	-	7h 7min
Case 2							
C2H1	48	34	0.3	39	55	42	6h 26min
C2D1	60	100	-	60	-373	-	6h 25min
C2H2	48	30	0.3	33	59	38	6h 26min
C2D2	53	100	-	48	-336	-	6h 25min
C2H3	48	26	0.3	37	77	35	6h 26min
C2D3	42	100	-	48	-316	-	6h 25min
C2H4	48	38	0.3	15	-7	41	6h 26min
C1D4	36	100	-	39	-461	-	6h 25min

4.5.2 Dehydration

Table 4.4 shows the results of planned dehydrations performed according to the operating conditions as mentioned in Table 3.3. The dehydration is stopped when the dehydration curve becomes horizontal at the end of the reaction, which indicates that the reaction is finished.

Case 1: Variable T_{in} and Constant GFC

By increasing the dehydration temperature from 70 °C–120 °C, it is observed that the amount of H_2O released, and energy absorbed are increased. It is possibly due to increased driving force by raising the air temperature at the inlet. At 70 °C in C1D1, 20 g of H_2O is released, and -193 kJ of energy is provided to the reactor. With 80 °C (C1D2), the amount of H_2O released is increased to 47 g. In C1D3, H_2O released is 40 g, which is 7 g less as compared to C1D2. It is because intermediate hydrations are performed at different operating conditions, which might result in less/more water absorbed in hydrations. Figure 4.20 shows that with the increase in dehydration temperature, the reaction speed is also increased.

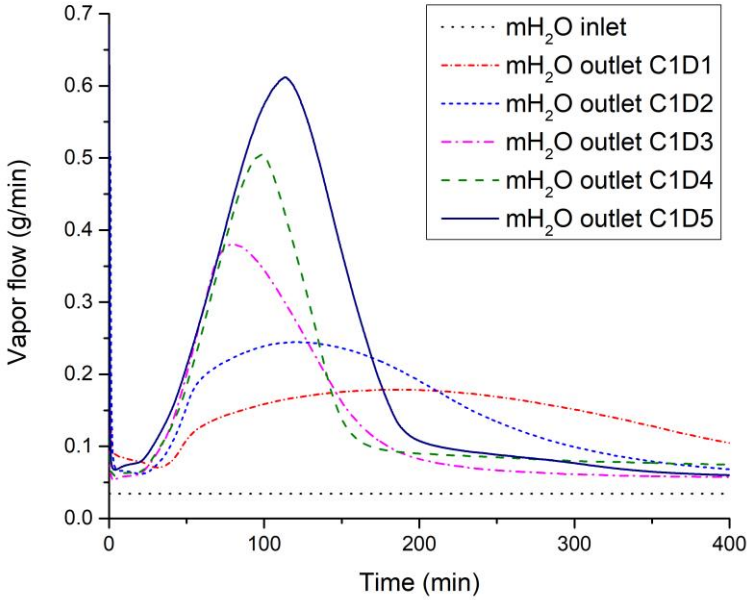

Figure 4.20: Comparison of case 1 dehydrations performed with variable reactor inlet air temperature, as mentioned in Table 3.3.

To investigate the low amount of water released at 70 °C (C1D1), reactor inlet wall temperatures (B1–B5) are plotted with the equilibrium temperature (T_{eq}). For the material to be completely dehydrated, the temperature must be above the T_{eq}. The inside wall temperature is lower than the bed temperature at the centre. This is because of the thermal losses to the reactor wall. Figure 4.21 shows that the temperature near the wall region is much lower than T_{eq}. This indicates that the material near the wall region is not dehydrated, and that is why the material released only 20 g in C1D1.

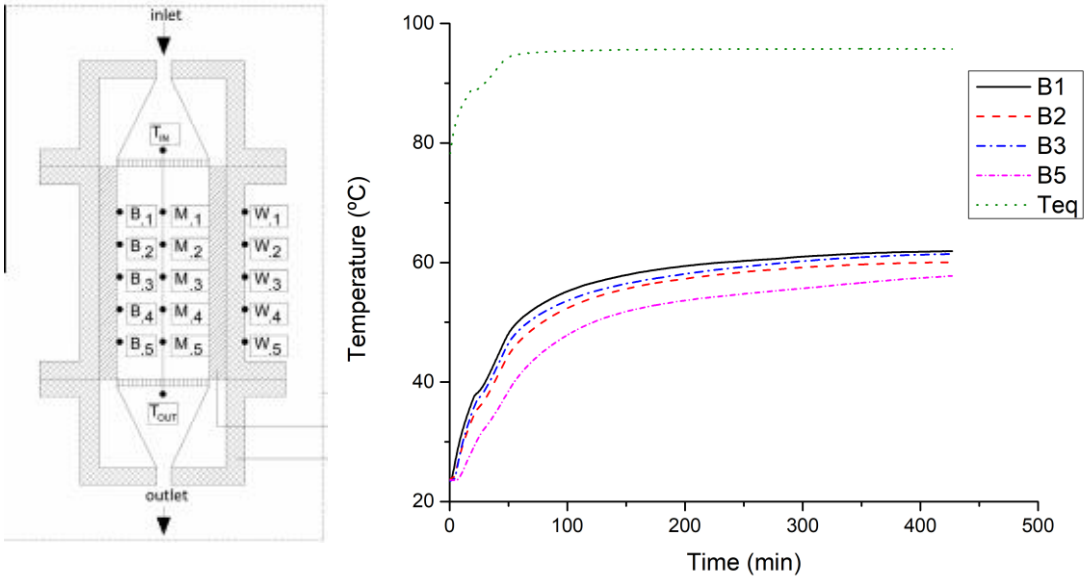

Figure 4.21: Reactor inside wall temperature (B1–B5) for $T_{dehydration}$ of 70 °C

Case 2: Variable GFC and Constant T_{in}

By decreasing the mass flow rate at the reactor inlet (GFC), the amount of H_2O released is decreased. One of the possible reason could be that with a higher mass flow rate of air, the hot air can penetrate relatively easily into the grain cracks and to those regions of the bed which have lower bed porosity, thereby essentially releasing more amount of H_2O. Figure 4.22 shows that with the increase of mass flow rate of air at the reactor inlet, the reaction speed is also increased.

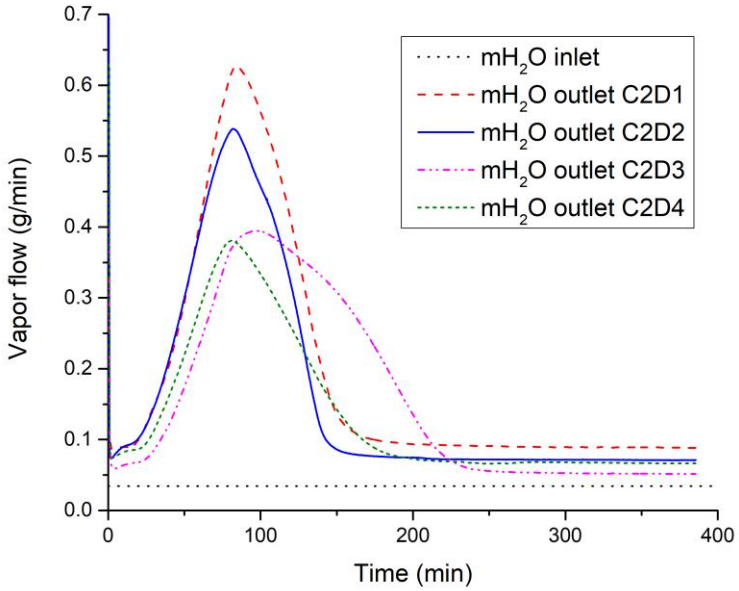

Figure 4.22: Comparison of case 2 dehydrations performed with a variable mass flow rate of air at the reactor inlet, as mentioned in Table 3.3.

4.5.3 Reactor Opening at the end of Experimental Phase

The reactor is opened at the end of the experimental phase to visually analyze the K_2CO_3 composite. Firstly, it is observed that the grains of material expanded after consecutive contraction and expansion during hydration/dehydration, which is also observed by Ferchaud [27] during the grain level investigation of $MgCl_2.6H_2O$. At the beginning of the experimental phase, the reactor was filled until the top of the reactor height, as shown in Figure 4.23 [Left]. At the end of the experimental phase, it is seen that the material expanded and is gathered at the top of the reactor, as shown in Figure 4.23 [Right].

Secondly, when the reactor is opened from the bottom, it is seen that the material did not fall because of agglomeration (Figure 4.24). It also proves the presence of dead zones due to minimal bed porosity. This is the reason why in phase 2 dehydration, the reactor outlet temperature was higher than the temperature at the bottom of the reactor.

Finally, the agglomeration of K_2CO_3 composite grains is found at the end of the experimental phase (Figure 4.25). This is possibly due to expansion and contraction of grains during consecutive hydration and dehydration, thereby forming dead zones at the reactor bottom.

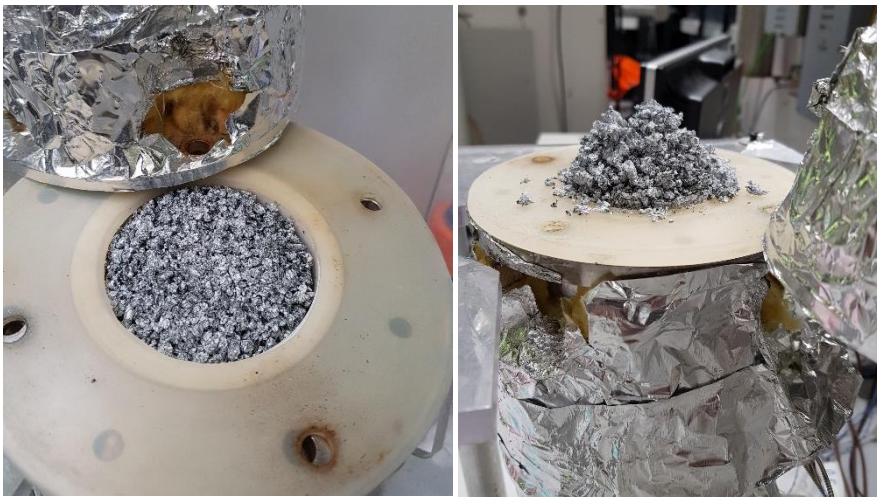

Figure 4.23: [Left] Before Experiments: The material filled until the top of reactor height [Right] After Experiments: The material expanded and settled at the top of the reactor

Figure 4.24: Presence of dead zones at the reactor bottom

Figure 4.25: Agglomeration of the K_2CO_3 composite at the end of an experimental phase

4.6 Experimental Reactor Performance

4.6.1 Experimental Temperature Lift in the Reactor

The hydrations are performed under different operating conditions. Hence, the temperature lifts obtained during the reaction are also different (Table 4.5). It varies between 28 °C–41 °C, whereas the theoretical temperature lift in the reactor is 41 °C.

Table 4.5: Maximum temperature lift in the reactor during all the hydrations

Case	Cyclic Experiments		Planned Experiments		
#	Phase 1 (°C)	Phase 2 (°C)	Variable C_{in} (°C)	Variable GFC (°C)	Variable T_{in} (°C)
1	36	39	38	28	42
2	31	38	-	29	38
3	32	36	-	33	35
4	33	36	-	39	41
5	31	-	-	-	-

4.6.2 Experimental Energy Density of the Reactor

In reference hydration, the amount of energy obtained from the reactor is 67 kJ (Table 4.2). The experimental energy density of reference hydration is calculated by dividing the volume occupied by the salt in the reactor and bed porosity during hydration (Equation 4.3). It must be noted that the reactor does not contain pure K_2CO_3. Hence, the percentage of inert material added to the composite is removed from the volume occupied by the composite in the reactor. The experimental energy density is 0.36 GJ/m^3 (calculated from Equation 4.3), which is much less as compared to theoretical energy density i.e. 0.6 GJ/m^3. The possible reasons for low energy density compared to theoretical energy density are a change in material kinetics during consecutive hydration/dehydration, mass and heat transfer losses, agglomeration and dead zones in the reactor bed.

$$Experimental\ Energy\ Density = \frac{67\ kJ}{4 \times 10^{-4}\ \mathrm{m}^3 \times (1 - 0.54)} = 0.36\ \frac{GJ}{m^3} \quad \text{Equation 4.3}$$

4.6.3 Experimental Overall Heat Transfer Coefficient

The aim of this section is to compare the theoretical (U_{Th}) and experimental overall heat transfer coefficient (U_{Exp}). At the end of preliminary dehydration, it is assumed that the dehydration is complete. If the dehydration reaction is finished, then the power absorbed due to endothermic reaction ($P_{reaction}$) and the amount of sensible heat transfer to the material ($P_{sensible}$) should be zero. Hence, Equation 3.11 can be reduced to:

$$P_{loss} = P_{convection} = \sum_{i=1}^{5} (\frac{T_{Bi} - T_{Wi}}{R}) A_i$$

Therefore, experimental heat resistance (R_{Exp}) is calculated by Equation 4.4.

$$R_{Exp} = \frac{(T_{B1} - T_{W1})A_1 + (T_{B2} - T_{W2})A_2 + (T_{B3} - T_{W3})A_3 + (T_{B5} - T_{W5})A_5}{P_{loss}} \quad \text{Equation 4.4}$$

Whereas, T_{Bi} and T_{Wi} are the inside and outside reactor wall temperatures. Thermocouple at the inside wall of the reactor (B4) was broken, therefore, it is not considered. A_i is the

area of each of the five segments in which the reactor is divided and P_{loss} is the instantaneous power loss at the end of preliminary dehydration. The values of these parameters at the end of preliminary dehydration are shown in Table 4.6.

Table 4.6: Values of T_{Bi}, T_{Wi} and A_i at the end of the preliminary dehydration

Bed Position#	T_{Bi} (°C)	T_{Wi} (°C)	A_i (m^2)
Bed 1	102	82	0.0044
Bed 2	96	84	0.0044
Bed 3	96	83	0.0044
Bed 5	90	82	0.0088

$$R_{Exp} = \frac{0.26}{2.27} = 0.11 \frac{m^2 \cdot K}{W} \text{ and } U_{Exp} = \frac{1}{R_{Exp}} = 9 \frac{W}{m^2 \cdot K} = U_{Th}$$

The experimental overall heat transfer coefficient (U_{Exp}) is 9 W/(m^2·K) which is also equal to U_{Th} (calculated from Equation 3.8).

Chapter 5 | Conclusions and recommendations

5.1 Conclusion

The aim of this research project was to investigate the performance of K_2CO_3 composite at reactor-scale. A literature review on sorption heat storage is done, both on material and prototype level to understand the current advancements. On material level, composite materials are promising due to their ability to provide structural stability. On prototype level, there exist some projects of sorption systems suitable for low-temperature applications focused both on open and closed systems. The reactor setup is studied to understand the working principle of different components. All the thermocouples are tested with the calibrator device for two different temperatures to realize their accuracy. The theoretical reactor outlet temperature is found to be 41 °C. Whereas experimentally it is found to be 36 °C for the reference hydration. The theoretical energy density of the reactor is 0.6 GJ/m^3. Whereas experimentally, it is found to be 0.36 GJ/m^3 for the reference hydration. The possible reasons of low energy density compared to theoretical energy density are a change in material kinetics during consecutive hydration/dehydration, mass and heat transfer losses, formation of dead zones at the reactor bottom, and side reactions with CO_2. The theoretical energy content of the reactor is 132 kJ, whereas experimentally it is only 67 kJ obtained at the end of a reference hydration. The particle size distribution of the K_2CO_3 composite (grain size up to 3 mm) is determined and it has been found that most of the grains lie within the range of 2 mm. The reactor is filled with 423 grams of K_2CO_3 composite. Experiments are classified into two categories: cyclic and planned.

5.1.1 Cyclic Experiments

Cyclic experiments are done in two phases, with two different sets of operating conditions. The aim is to understand the cyclability of K_2CO_3 composite after consecutive cycles of hydration and dehydration. In phase 1 experiments, the K_2CO_3 composite absorbed and released roughly twice less H_2O than phase 2 experiments. This effect is possibly due to low driving force. It is also seen that the energy and water absorbed or released are reduced in consecutive cycles, which may be due to the slow material kinetics, as discussed by Ferchaud et. al [27], while investigating $MgSO_4$ salt hydrate. It is noted from both phase 1 and 2 cyclic experiments that the amount of H_2O released in each dehydration is higher than absorbed in previous hydration (see Table 4.2 and Table 4.3). This is because the experiments are reduced to 5 h 6 min. The material will possibly continue to absorb water after 5 h 6 min during hydration. But probably due to the slow kinetics of the material, the material takes up only a small portion of water in 5 h 6 min. Conversely, during dehydration, the material is releasing more water in 5 h 6 min. Also, reactor leakage test is done and found that there are air leakages in the reactor. Efforts are made during the project to reduce the air leakages but still the reactor could not be made completely airtight. The reactor is cooled overnight and due to these leakages, the air might have entered during overnight cooling, which might be one of the possible reasons of more H_2O released in dehydration than previous hydration. However, it is just a hypothesis and no calculations are done for quantifying the amount of water absorbed by the material in the reactor during overnight cooling.

In phase 2 experiments, the water content per cycle is improved than phase 1 experiments. This is possibly due to increased driving force (from 0.3 mol/m^3 to 0.4 mol/m^3). Also, due to consecutive expansion and contraction of the grains over cycles, cracks might have developed due to which the area of reaction (reaction interface) increases and the water flow in and out of the grain (water vapor diffusion) becomes easier [27]. The last three

hydrations (P2H2, P2H3, P2H4) replicate nearly similar results in terms of water content (48 g of H_2O absorbed in 5 h 6 min), as can be seen in Table 4.3. Hence, it may be concluded that the K_2CO_3 composite has attained a cyclic nature due to the production of similar results in hydrations. Also, at the end of phase 2 experiments, an evidence of the formation of dead zones is found at the bottom of the reactor.

5.1.2 Planned Experiments

The kinetic performance of K_2CO_3 composite is analyzed under variable operating conditions. In hydration, experiments are performed according to the operating conditions mentioned in Table 3.3. From the results of Table 4.4, the following conclusions may be derived:

- With the increased water vapor concentration at the reactor inlet from 0.3 mol/m^3 (Ref hydration) to 0.4 mol/m^3 (C3H1), the amount of water absorbed is increased by 34% and the energy released during hydration reaction is increased by 43%.
- With the increased mass flow rate of air at reactor inlet from 36 g/min (C1H4) to 60 g/min (C1H1), the amount of water absorbed is decreased by 67%. It must be noted that intermediate dehydrations are performed at different temperatures, which might have affected the amount of water absorbed in the following hydration.
- With the increased inlet air temperature from 26 °C (C2H3) –36 °C (C2H1), the amount of water absorbed is decreased by 60 %. This is because, at higher inlet air temperature, the material is also releasing the amount of water absorbed during hydration.

In dehydration, experiments are performed according to the operating conditions mentioned in Table 3.3. From the results of Table 4.4, following conclusions may be derived:

- With the increased reactor dehydration temperature from 70 °C (C1D1) to 120 °C (C1D5), the amount of water released is increased from 20 g to 55 g (175%). This is because at higher temperature, the driving force to remove water is high. Also, with the lower dehydration temperature, the inside wall temperature is lower due to thermal losses to the wall. Hence, it is possible that the material near the wall region is not completely dehydrated and thereby less amount of water is removed during lower dehydration temperatures. It must be noted that the hydrations performed in between dehydrations are at variable inlet air flow rate i.e. from 36 g/min to 60 g/min.
- With the increased mass flow rate of air (GFC) from 36 g/min (C2D4) to 60 g/min (C2D1), the amount of water released is increased by 54%. But it should be noted that the hydrations, in between case 2 dehydrations, are performed at variable inlet air temperature i.e. from 26 °C –38 °C.

5.2 Challenges and Recommendations

The experiments performed on the lab-scale reactor setup have highlighted several challenges and drawbacks of the setup. The following section explains the drawbacks and possible recommendations to solve them.

5.2.1 Guidelines for Reactor Design Improvement

The current design of reactor presented numerous challenges during the experimental phase of this research project.

- The reactor was not completely airtight prior to this project, which is critical for the hydration/dehydration of materials that have the affinity to absorb water when exposed to ambient environment. It can lead to the deliquescence of the material.

Prior to the hydration/dehydration reaction, the reactor is required to cool to the ambient temperature, which takes overnight time. If the reactor is not airtight, the salt hydrate would absorb extra moisture from the environment after hydrations, which would result in deliquescence. Efforts have been made during this project to make the reactor airtight. For instance, the screws of thermocouples on the outside of the reactor wall are tightened. The reactor walls are properly insulated with glass wool. An extra layer of rubber material equal to reactor diameter is placed at the top of the reactor to prevent air leakages from the top. Before, the addition of this layer, there were pressure losses from the reactor top. A pressure gauge is mounted to the side of the reactor to check the pressure losses within the reactor. After improvements, the pressure losses are reduced.

- The screws on the reactor housing, are mounted on places which are difficult to reach with screwdrivers. This results in less tightened screws and air leakage.

Therefore, if possible, a new reactor must be designed to avoid the above-mentioned design restrictions.

5.2.2 Controlled Evaporator Mixture (CEM) Module Temperature Control Valve & Heater

Bronkhorst® Software Set-point Issue

Prior to this research project, the CEM temperature control valve and heater were not used to set the desired inlet reactor conditions for hydrations e.g. concentration, temperature etc. One of the reasons being the use of a stable material i.e. zeolite, which was used previously for hydration/dehydration experiments at reactor-scale. But with a sensitive material like salt hydrates, certain inlet boundary conditions must be defined at the reactor inlet to avoid deliquescence. To that aim, a planned experimental campaign was developed to avoid these conditions, but due to the limitations of set-point value in the Bronkhorst® software, the experimental plan was modified, and the number of hydration experiments was reduced. The set-point percentage value for CEM heater could not be entered in decimals in the Bronkhorst® software.

Fluctuations of CEM heater

The CEM module heater is regulated by a temperature-controlled valve, which performs continuous on/off function to maintain an average desired reactor inlet temperature. However, constant on/off nature of control valve shows significant fluctuations, which are also visible, when graphs are made after completing hydration/dehydration experiments.

One of the possible ways to reduce the heater fluctuations is to add a long tube after the CEM module and before dehydration path without insulation. This would allow the mixture of air and water vapor after CEM to travel for a considerable amount of time within the long tube, which may result into a constant desired reactor inlet temperature. The feasibility of this possible modification was asked from the laboratory personnel and concluded that it is possible, but due to time limitations of the project, the above-mentioned idea was not implemented.

5.2.3 Sensors Calibration

In this project, the thermocouples are tested for only two different temperatures. All the thermocouples gave approximately the same temperature as set on the calibrator device. However, the thermocouples should be tested again for several different temperatures and calibrated again.

The humidity sensor is placed at the reactor outlet after the cooling circuit. It is sensitive to dust particles and high temperatures. It must be checked, cleaned and calibrated again for the accurate humidity measurement.

It is also recommended to place a humidity sensor at the reactor inlet to measure the accurate humidity (RH) and inlet water vapor concentration (C_{in}). In this project, both RH and C_{in} are theoretically calculated.

5.2.4 Actual Temperature for CEM Set-point

The set-point percentage entered in the Bronkhorst® software should correspond to a specific temperature of the heater. This will allow an individual to set a desired temperature at the reactor inlet for hydration experiments. For the current project, a cumbersome reverse-engineering was done to determine, which percentage of software set-point corresponds to which reactor inlet temperature.

A CEM heater catalog must be provided by Bronkhorst® to have exact information of set-point versus reactor inlet temperature.

5.2.5 PLW Recorder

During this research project, on numerous occasions, PLW recorder stopped showing readings of thermocouples and it showed errors of not detecting the thermocouples attached to the Pico log housing.

The updated version of PLW recorder must be installed to avoid the above-mentioned issue.

References

[1] B. N. Stram, "Key challenges to expanding renewable energy," *Energy Policy*, vol. 96, pp. 728–734, 2016.

[2] M. Building and E. Codes, "Modernising building energy codes to secure our global energy future.," 2013.

[3] D. Roadmap, "Solar heating and cooling for a sustainable energy future in europe (revised)."

[4] CBS, *National accounts of the Netherlands 2008*. 2009.

[5] "Top 6 Things You Didn't Know About Solar Energy | Department of Energy." [Online]. Available: https://energy.gov/articles/top-6-things-you-didnt-know-about-solar-energy. [Accessed: 07-Feb-2018].

[6] "Koninklijk nederlands meteorologisch instituut (knmi)." [Online]. Available: http://www.knmi.nl/research. [Accessed: 07-Feb-2018].

[7] "Centraal bureau voor de statistiek (cbs)." [Online]. Available: https://www.cbs.nl/en-gb/figures. [Accessed: 07-Feb-2018].

[8] T. Schmidt and O. Miedaner, "Storage," *Sol. Dist. Heat. Guidel.*, pp. 1–13, 2012.

[9] *Heat and cold storage with PCM -An up to date introduction into basics and applications*. Berlin, Heidelberg: Springer Berlin Heidelberg, 2008.

[10] L. F. Cabeza, *Advances in thermal energy storage systems : methods and applications*. .

[11] J.-C. Hadorn, *Thermal energy storage for solar and low energy buildings, IEA Solar Heating and Cooling Program, task 32, 2005*. University of Lleida, 2005.

[12] F. Salaun, "Polymer nanoparticles to decrease thermal conductivity of phase change materials." .

[13] B. Mette, H. Kerskes, H. Drück, and H. Müller-Steinhagen, "New highly efficient regeneration process for thermochemical energy storage," *Appl. Energy*, vol. 109, pp. 352–359, 2013.

[14] Gaeini, *Thermochemical seasonal heat storage for the built environment*. 2017.

[15] S. Brunold, R. Frey, and U. Frei, "Comparison of three different collectors for process heat applications," *SPIE 2255, Opt. Mater. Technol. Energy Effic. Sol. Energy Convers. XIII*, vol. 2255, no. September 1994, pp. 107–118, 1994.

[16] B. Fumey, R. Weber, P. Gantenbein, X. Daguenet-Frick, T. Williamson, and V. Dorer, "Closed sorption heat storage based on aqueous sodium hydroxide," *Energy Procedia*, vol. 48, pp. 337–346, 2014.

[17] H. Kerskes and K. Sommer, "MonoSorp Integrales Konzept zur solarthermischen Gebäudeheizung mit MonoSorp," no. September, 2007.

[18] Y. Sakamoto and H. Yamamoto, "Performance of Thermal Energy Storage Unit Using Solid Ammoniated Salt (CaCl2-NH3 System)," *Nat. Resour.*, vol. 05, no. 08, pp. 337–342, 2014.

[19] N. Yu, R. Z. Wang, and L. W. Wang, "Sorption thermal storage for solar energy," *Prog. Energy Combust. Sci.*, vol. 39, no. 5, pp. 489–514, 2013.

[20] K. E. N'Tsoukpoe, H. Liu, N. Le Pierrès, and L. Luo, "A review on long-term sorption solar energy storage," *Renew. Sustain. Energy Rev.*, vol. 13, no. 9, pp. 2385–2396, 2009.

[21] D. Aydin, S. P. Casey, and S. Riffat, "The latest advancements on thermochemical heat storage systems," *Renew. Sustain. Energy Rev.*, vol. 41, pp. 356–367, 2015.

[22] G. Ervin, "Solar heat storage using chemical reactions," *J. Solid State Chem.*, vol. 22, no. 1, pp. 51–61, 1977.

[23] L. Scapino, H. A. Zondag, J. Van Bael, J. Diriken, and C. C. M. Rindt, "Sorption heat storage for long-term low-temperature applications: A review on the advancements at material and prototype scale," *Appl. Energy*, vol. 190, pp. 920–948, 2017.

[24] V. M. van Essen *et al.*, "Characterization of MgSO Hydrate for Thermochemical Seasonal Heat Storage," *J. Sol. Energy Eng.*, vol. 131, no. 4, p. 041014, 2009.

[25] V. M. van Essen *et al.*, "Characterization of Salt Hydrates for Compact Seasonal Thermochemical Storage," *ASME 2009 3rd Int. Conf. Energy Sustain. Vol. 2*, vol. 2, pp. 825–830, 2009.

[26] C. Ferchaud, H. Zondag, R. De Boer, and C. Rindt, "Characterization of the sorption process in thermochemical materials for seasonal solar heat storage application," *Proc. 12th Int. Conf. Energy Storage*, pp. 1–10, 2012.

[27] C. J. Ferchaud, R. A. A. Scherpenborg, H. A. Zondag, and R. De Boer, "Thermochemical seasonal solar heat storage in salt hydrates for residential applications - influence of the water vapor pressure on the desorption kinetics of MgSO4·7H2O," *Energy Procedia*, vol. 57, pp. 2436–2440, 2014.

[28] C. Ferchaud, *Experimental study of salt hydrates for thermochemical seasonal heat storage*. Technische Universiteit Eindhoven, 2016.

[29] P. A. J. Donkers, L. Pel, and O. C. G. Adan, "Experimental studies for the cyclability of salt hydrates for thermochemical heat storage," *J. Energy Storage*, vol. 5, pp. 25–32, 2016.

[30] "Method of storing energy and system for carrying out this method," Jun. 1981.

[31] Brunberg E-Å, "Double-duty heat pump stores chemical heat too. [Tepidus system]," *J. Energy*, vol. 5, no. 4, pp. 214–217, Jul. 1981.

[32] R. de Boer, W. . Haije, and J. B. . Veldhuis, "Determination of structural, thermodynamic and phase properties in the Na2S–H2O system for application in a chemical heat pump," *Thermochim. Acta*, vol. 395, no. 1–2, pp. 3–19, 2002.

[33] R. Boer *et al.*, "Solid-Sorption Cooling With Integrated Thermal Storage: The SWEAT Prototype," *Int. Conf. Heat Powerd Cycles, Larnaca, Cyprus*, no. August, 2004.

[34] F. Trausel, A. J. De Jong, and R. Cuypers, "A review on the properties of salt hydrates for thermochemical storage," *Energy Procedia*, vol. 48, pp. 447–452, 2014.

[35] V. M. van Essen *et al.*, "Characterization of MgSO[sub 4] Hydrate for Thermochemical Seasonal Heat Storage," *J. Sol. Energy Eng.*, vol. 131, no. 4, p. 041014, 2009.

[36] F. Bertsch, B. Mette, S. Asenbeck, H. Kerskes, and H. Müller-Steinhagen, "Low temperature chemical heat storage – an investigation of hydration reactions," *Effstock Conf. Stock.*, no. June, pp. 1–8, 2009.

[37] B. Michel, N. Mazet, S. Mauran, D. Stitou, and J. Xu, “Thermochemical process for seasonal storage of solar energy: Characterization and modeling of a high density reactive bed,” *Energy*, vol. 47, no. 1, pp. 553–563, 2012.

[38] B. Michel, N. Mazet, and P. Neveu, “Experimental investigation of an innovative thermochemical process operating with a hydrate salt and moist air for thermal storage of solar energy: Global performance,” *Appl. Energy*, vol. 129, pp. 177–186, 2014.

[39] S. P. Casey, J. Elvins, S. Riffat, and A. Robinson, “Salt impregnated desiccant matrices for ‘open’ thermochemical energy storage - Selection, synthesis and characterisation of candidate materials,” *Energy Build.*, vol. 84, pp. 412–425, 2014.

[40] M. M. Druske *et al.*, “Developed materials for thermal energy storage: Synthesis and characterization,” *Energy Procedia*, vol. 61, pp. 96–99, 2014.

[41] H. Liu, K. Nagano, and J. Togawa, “A composite material made of mesoporous siliceous shale impregnated with lithium chloride for an open sorption thermal energy storage system,” *Sol. Energy*, vol. 111, pp. 186–200, 2015.

[42] O. Opel, H. . Rammelburg, M. Gerard, and W. Ruck, “Thermochemical Storage Materials Research - Tga / Dsc-Hydration Studies,” 2006.

[43] L. Greenspan, “Humidity fixed points of binary saturated aqueous solutions,” *J. Res. Natl. Bur. Stand. Sect. A Phys. Chem.*, vol. 81A, no. 1, p. 89, 1977.

[44] H. A. Zondag, *Thermal energy storage course*. 2017.

[45] I. The MathWorks, “MatLab R2016 b.” The MathWorks, Inc., Natick, Massachusetts, United States, 2016.

[46] P. A. J. Donkers, L. C. Sögütoglu, H. P. Huinink, H. R. Fischer, and O. C. G. Adan, “A review of salt hydrates for seasonal heat storage in domestic applications,” *Appl. Energy*, vol. 199, pp. 45–68, 2017.

[47] Craig B and B. Anderson, *Handbook of Corrosion Data*. 1995.

[48] M. Roelands *et al.*, “Preparation & Characterization of Sodium Sulfide Hydrates for Application in Thermochemical Storage Systems,” *Energy Procedia*, vol. 70, no. 0, pp. 257–266, 2015.

[49] T. Joosten, “Analysis large scale reactor design in thermo- chemical heat storage,” no. April, 2014.

[50] A. Hauer, “Thermal energy storage with zeolite for heating and cooling applications,” *2nd Int heat powered cycles conf - cool heat power gener syst, Paris*, 2001. [Online]. Available: https://tue.on.worldcat.org/atoztitles/link?url_ver=Z39.88-2003&ctx_ver=Z39.88-2003&ctx_enc=info:ofi/enc:UTF-8&rft_id=info:doi/&rft_val_fmt=info:ofi/fmt:kev:mtx:journal&rft.aulast=Hauer&rft.aufirst=A.&rft.issn=&rft.isbn=&rft.volume=&rft.issue=&rft.date=20. [Accessed: 04-Mar-2018].

[51] C. Bales *et al.*, “Laboratory Tests of Chemical Reactions and Prototype Sorption Storage Units,” *A Rep. IEA Sol. Heat. Cool. Program. - Task 32 Adv. storage concepts Sol. low energy Build.*, no. December, p. 55p., 2008.

[52] H. a Zondag, V. M. van Essen, L. P. J. Bleijendaal, B. W. J. Kikkert, and M. Bakker, “Application of MgCl2· 6H2O for thermochemical seasonal solar heat storage,” *5th*

IRES Conf., no. NOVEMBER, pp. 22–24, 2011.

[53] H. Paksoy, *Thermal Energy Storage for Sustainable Energy Consumption, Fundamentals, Case Studies and Design*. 2005.

[54] D. Jähnig, R. Hausner, W. Wagner, and C. Isaksson, "Thermo-chemical storage for solar space heating in a single-family house," *AEE – INTEC (Austria), Ecostock Conf. New Jersey; 31 May - 02 June*, pp. 1–7, 2006.

[55] E+E Elektronik Ges.m.b.H, "Manual Hardware and Software of Humidity/Temperature Transmitter Series EE33."

[56] a. J. Brouwer, "Development of an experimental device for the investigation of seasonal heat storage by thermo-chemical materials," 2008.

[57] P. A. J. Donkers, L. C. Sögütoglu, H. P. Huinink, H. R. Fischer, and O. C. G. Adan, "A review of salt hydrates for seasonal heat storage in domestic applications," *Appl. Energy*, vol. 199, pp. 45–68, 2017.

[58] W. Renewables, "Solar Thermal Collector Types."

[59] L. C. Sögütoglu, P. A. J. Donkers, H. R. Fischer, H. P. Huinink, and O. C. G. Adan, "In-depth investigation of thermochemical performance in a heat battery : Cyclic analysis of K 2CO3 , MgCl2 and Na2S," vol. 215, no. August 2017, pp. 159–173, 2018.

[60] H. Luo, H. Chioyama, S. Thürmer, T. Ohba, and H. Kanoh, "Kinetics and Structural Changes in CO2 Capture of K2CO3 under a Moist Condition," *Energy & Fuels*, vol. 29, no. 7, pp. 4472–4478, 2015.

[61] W. Dong, X. Chen, Y. Wu, C. Zhao, and C. Liang, "Carbonation characteristics of dry sodium-based sorbents for CO2 capture," *Energy and Fuels*, vol. 26, no. 9, pp. 6040–6046, 2012.

[62] "Thermocouple Accuracies." [Online]. Available: https://www.thermocoupleinfo.com/thermocouple-accuracies.htm.

[63] H. Ahn, M. B. Kim, and C. H. Lee, "Effects of heat-transfer coefficients on thermal dynamics in a near-adiabatic fixed bed," *Sep. Sci. Technol.*, vol. 39, no. 11, pp. 2627–2654, 2004.

[64] F. Incropera and D. DeWitt, *Fundamentals of Heat and Mass Transfer*. John Wiley & Sons: New York, NY, USA, 1996.

[65] F. White, *Heat and Mass Transfer*. 1998.

[66] M. Ozisik, *Heat Transfer*. McGraw-Hill: New York, NY, USA, 1985.

[67] G. L. Shires, "Prandtl Number," in *Guide to Thermodynamics, Heat and Mass Transfer, and Fluids Engineering*, Begellhouse.

[68] O. Reynolds, "An experimental investigation of the circumstances which determine whether the motion of water shall be direct or sinuous and of the law of resistance in parallel channels," *Philos. Trans. R. Soc. London*, vol. 174, no. 1883, pp. 935–982.

[69] G. L. Shires, "Reynolds Number," in *Guide to Thermodynamics, Heat and Mass Transfer, and Fluids Engineering*, Begellhouse.

Appendix

Appendix A

Calculation of $T_{equilibrium}$

For the dehydration temperature range of 70–120 °C, it is important to justify that dehydration occurs at these operating conditions. According to Antoine Equation, with Antoine constants valid for $T_{maximum} = 100$ °C, the $P_{saturation}$ at 70 °C is given as:

$$P_{saturation} = 10\text{^}[8.07131 - \frac{1730.63}{233.426 + T_{dehydraiton}}] = 31087Pa$$

The grid air contains 2.5% of relative humidity, therefore the water vapor pressure (P_{H_2O}) is calculated as:

$$P_{H_2O} = \frac{P_{saturation} * RH}{100} = 777\ Pa = 7.7\ mbar$$

From Figure A.1, at 7.7 mbar, the $T_{equilibrium}$ is 52 °C. This indicates that the point of 7.7 mbar at 70 °C, lies below the red line and dehydration will occur. This calculation justifies that the range considered for dehydration temperature is theoretically correct.

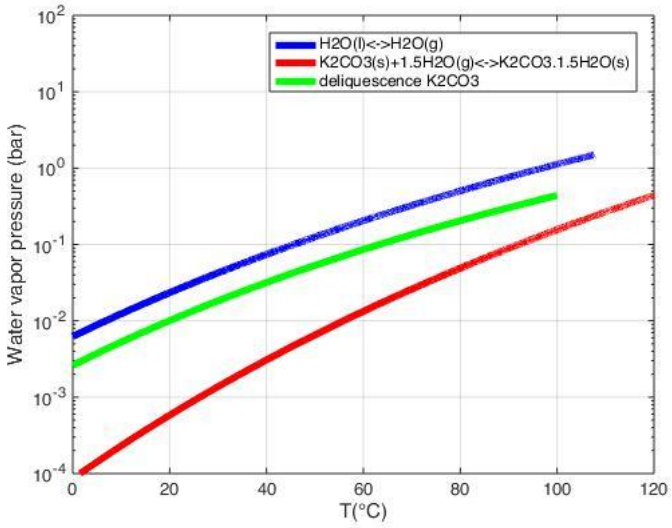

Figure A.1: The phase diagram of K_2CO_3

Appendix B
Thermocouple Testing

The thermocouples are tested using a calibrator device filled with distilled water. It is set at a temperature of 30 °C initially and later at 89 °C. To confirm that the calibrator device is showing the right temperature, the mercury thermometer is also placed in water, which gave 30 °C and 89 °C as well. All the thermocouples are placed in the water for half an hour to settle down the frequent fluctuations in temperature readings. All the thermocouples gave almost the same temperature as on the calibrator device except M2, which was found to be broken. The results of all the thermocouples are shown in Table B.1.

Table B.1: Calibration of all the thermocouples

Thermocouples	Calibrator device set at 30 °C	Calibrator device set at 89 °C
T1	30.3	89.2
T2	30.5	89.4
B1	30.2	89.1
B2	30.1	89.2
B3	29.9	88.8
B4	29.7	90.4
B5	29.7	89.1
M1	30.5	89.8
M2	22.8	-
M3	29.7	89.6
M4	29.9	89.1
M5	29.9	90

Appendix C
Internal Convective Heat Transfer Coefficient Calculation

The convective heat transfer coefficient is calculated by Equation C.1. According to Ahn et al. [63], the correlation between the Nusselt and Reynolds number for the heat transfer of flow in a circular tube can be considered for estimating the heat transfer in a packed bed.

$$h = \frac{Nu\ \lambda_{air}}{D} \qquad \text{Equation C.1}$$

Where λ_{air} is the thermal conductivity of air, D is the internal reactor diameter and Nu is the Nusselt number, which is given by Equation C.2.

$$Nu = 0.309\ Re^{0.8} Pr \qquad \text{Equation C.2}$$

Where Re is the Reynolds number in the porous media, defined by Equation C.3 and Pr is the Prandtl number given by Equation C.4.

$$Re = \frac{d_p\ u\ \rho_{air}}{\mu_{air}(1-\epsilon_b)} \qquad \text{Equation C.3}$$

Where dp is the particle diameter of K_2CO_3 composite, u is the air velocity at the reactor inlet, ρ_{air} is the air density, μ_{air} is the air viscosity and ϵ_b is the bed porosity.

$$Pr = \frac{C_{p_{air}}\ \mu_{air}}{\lambda_{air}} \qquad \text{Equation C.4}$$

Where, $C_{p_{air}}$ is the specific heat capacity of air. The velocity of air is calculated (Equation C.5) from the mass flow rate of air at reactor inlet (GFC) and the cross-sectional area of the body of the reactor (A_w).

$$u = \frac{GFC}{A_w} \qquad \text{Equation C.5}$$

The bed porosity is determined from the bed density (ρ_{bed}) and particle density ($\rho_{particle}$) by Equation C.6, whereas bed density is calculated as a ratio of mass by the volume occupied by K_2CO_3 composite in the reactor (Equation C.7).

$$\epsilon_b = 1 - \frac{\rho_{bed}}{\rho_{particle}} \qquad \text{Equation C.6}$$

$$\rho_{bed} = \frac{m_{K_2CO_3}}{V_{K_2CO_3}} \qquad \text{Equation C.7}$$

The values of all the parameters involved in the calculation of the convective heat transfer coefficient of air (h) are present in Appendix H.

Appendix D
Dimensionless numbers – Significance

D.1 Nusselt Number

Nusselt number, *Nu,* is a dimensionless parameter that characterizes heat transfer by convection. According to Ahn et al. [63] the correlation between the Nusselt and Reynolds number (for the heat transfer of flow in a circular tube can be considered for estimating the heat transfer in a packed bed.

$$Nu = 0.309\, Re^{0.8}\,\mathrm{Pr} = h_{air}\,\frac{D}{k_{air}} \qquad \text{Equation D.1}$$

where *h, D* and *k* represent convective heat transfer coefficient of air, the inner diameter of the reactor and thermal conductivity of air respectively.

The significance of the *Nu* is discussed by numerous authors and agreed that certain useful information is associated with *Nu*. Incropera [64], considered *Nu* to be a dimensionless temperature gradient at the surface, which provides a measure of the convective heat transfer occurring at the surface. Also, the *Nu* is to the thermal boundary layer what the friction coefficient is to the velocity boundary layer. White [65], concludes the traditional dimensionless form of *h* is the *Nu,* which is defined as the ratio of convection heat transfer to fluid conduction heat transfer under the same conditions. Ozisik [66] interpreted *Nu* as the ratio of heat transfer by convection to conduction across the fluid layer of thickness *D.*

D.2 Prandtl number

Prandtl number, *Pr*, is another dimensionless parameter used during reactor numerical model, which characterizes the ratio of momentum diffusion to heat diffusion in a fluid and is expressed by Equation D.2.

$$\mathrm{Pr} = \frac{C_p \mu}{k} \qquad \text{Equation D.2}$$

where μ and *k* represent the air viscosity and thermal conductivity of air.

The *Pr* provides information about the speed of thermal diffusion in contrast to momentum diffusion. It also explains the relative thickness of thermal and momentum boundary layers. If momentum diffusion dominates thermal diffusion, this signifies that the fluid has a higher *Pr* number and vice versa. In fluids, the liquids generally offer high *Pr* number, which can be as high as 10^5 for some oils [67].

D.3 Reynolds number

Reynolds number, *Re*, is a dimensionless parameter that differentiates between laminar and turbulent flow and was first introduced by Osborne Reynolds in 1883 [68]. It is generally

used in the correlation of convective heat and mass transfer, and frictional pressure drop. It is expressed by Equation D.3.

$$Re = \frac{d_p u \rho_g}{\mu_g (1 - \epsilon_b)} \qquad \text{Equation D.3}$$

where d_p is particle diameter, u is air velocity entering the reactor, ρ_g is air density, μ_g is air viscosity and ϵ_b is bed porosity.

The *Re* provides the ratio of force associated with momentum to force associated with viscous shear [69]. The flow is said to be laminar or streamline if the *Re* is below a lower critical value. Alternatively, the flow is said to be turbulent or sinuous if the *Re* is above a higher critical value.

Appendix E
Cyclic Experiments

E.1 Original Time of Phase 1 Experiments

The experiments in phase 1 are performed for different time durations and the lengths of original time are shown in Table E.1.

Table E.1: The length of original time of phase 1 experiments

Phase 1 Exp#	Experiment	Time min
PID0	Dehydration	17hr 23min
P1H1	Hydration	7hr 31min
P1D1	Dehydration	7hr 37min
P1H2	Hydration	5hr 6min
P1D2	Dehydration	8hr 27min
P1H3	Hydration	5hr 42min
P1D4	Dehydration	5hr 9min
P1H4	Hydration	5hr 36min
P1D4	Dehydration	3hr 24min
P1H5	Hydration	3hr 24min

E.2 Original Time of Phase 2 Experiments

The experiments in phase 2 are performed for different time durations and the lengths of original time are shown in Table E.2.

Table E.2: The length of original time of phase 2 experiments

Phase 2 Exp#	Experiment	Time min
P2D1	Dehydration	3hr 30min
P2H1	Hydration	7hr 47min
P2D2	Dehydration	7hr 45min
P2H2	Hydration	8hr
P2D3	Dehydration	6hr 35min
P2H3	Hydration	7hr 21min
P2D4	Dehydration	6hr 31min
P2H4	Hydration	9hr 34min

Appendix F
Graphs of Phase 2 Dehydrations

In phase 2, the last three dehydrations (P2D2, P2D3, P2D4) reveal that reactor outlet temperature (T2) is higher than the lowest bed temperature (M5). Conversely, T2 should be lower than M5 because it is placed outside the reactor. This illustrates that probably some dead zones are formed at the reactor bottom, and the hot air is bypassed due to which T2 > M5, as shown in Figure F.1 and Figure F.2.

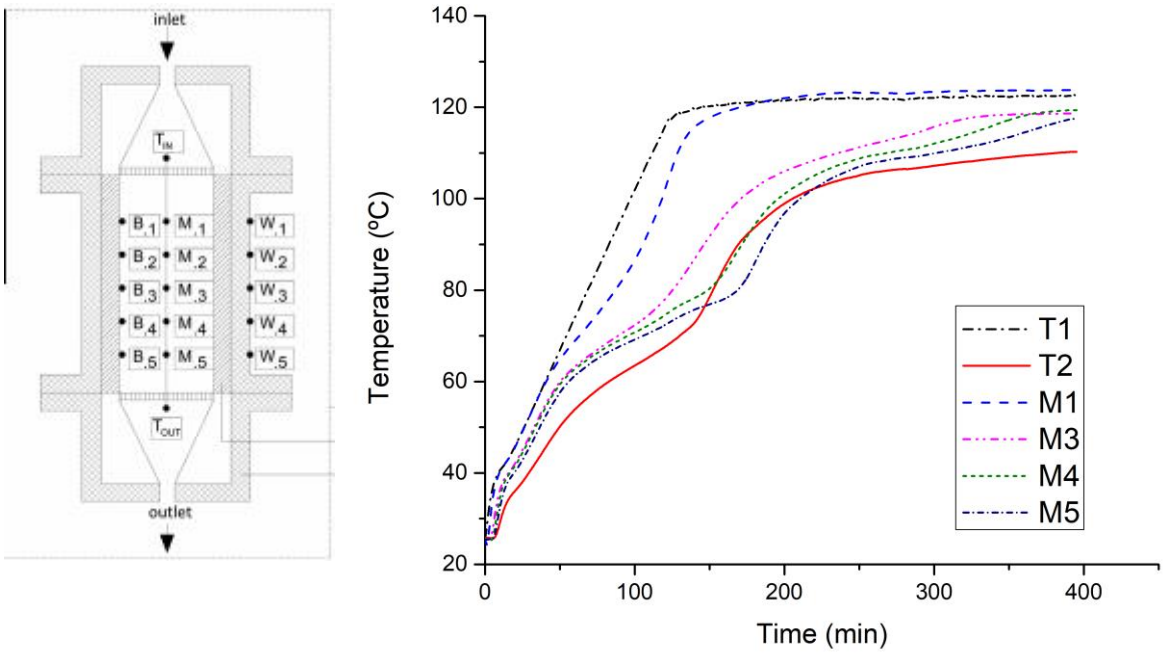

Figure F.1: P2D3 (Phase 2 Dehydration 3). Some dead zones are formed at the reactor bottom, and the hot air is bypassed due to which T2 > M5.

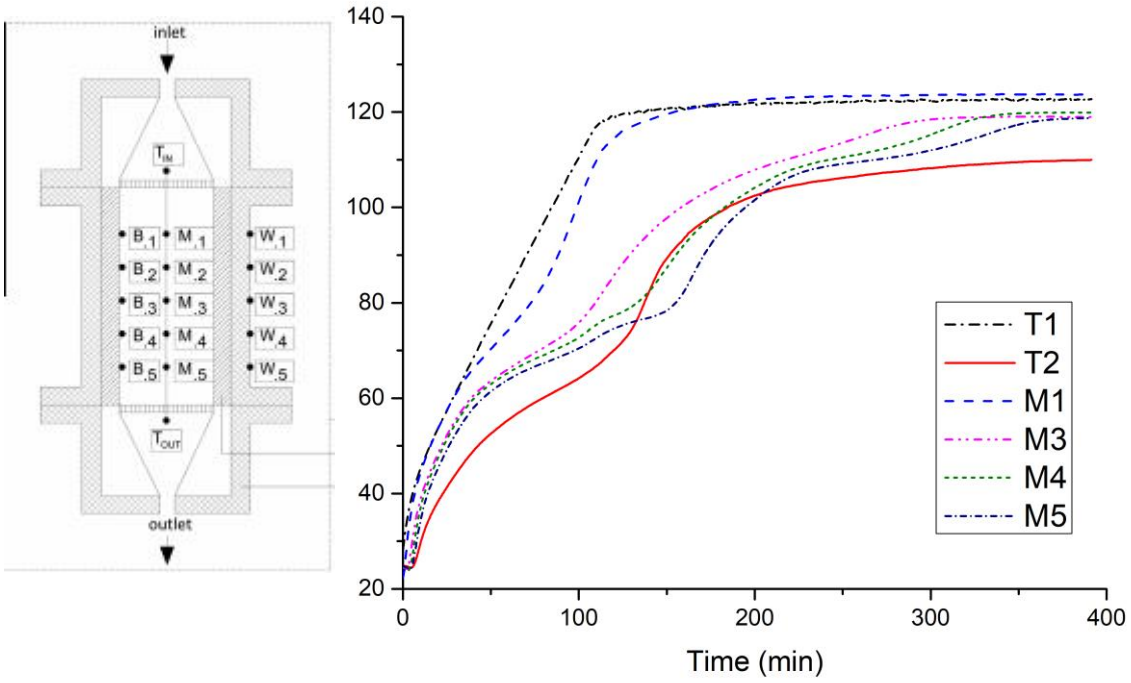

Figure F.2: P2D4 (Phase 2 Dehydration 4). Some dead zones are formed at the reactor bottom, and the hot air is bypassed due to which T2 > M5.

Appendix G
System Operation

A complete guide for the reactor-setup is provided for the proper operation. While working, there are certain important conditions which must be kept in mind for the safe operation. Firstly, during dehydration, the heater must be turned on only when there is an air flow through it, to prevent burn out of the heater. In this project, a software code is designed and integrated with the system that automatically turns off the heater when there is no air flow through it. Secondly, during hydration, the air pressure from the grid should be higher than of the liquid circuit to prevent the contamination of the gas circuit. In all the hydrations, the pressure of air and liquid flow is set as 7.5 bar and 6 bars respectively. Also, the water vessel in the liquid circuit is filled with distilled water and it must be ¾ of the height of the water vessel. Finally, during hydration, the Gas Flow Controller (GFC) must be opened before the Liquid Flow Controller (LFC). Figure G.1 shows the valve positions, which will help to understand the operation procedure. There are few valves which should be given special attention while operation.

- Valve 3, 10 and 11 are regulated by the Bronkhorst® software. A desireable set-point is selected in percentage for the air flow, liquid flow and the CEM heater. For a given setpoint percentage, there is a corresponding value of GFC and LFC in l_n/min in the catalog. However, no catalog is provided for the corresponding values of the CEM heater setpoints. It can be found simply by putting the percentage setpoint in the Bronkhorst® software and note down the temperature displayed on the CEM.
- Valve 1 is opened by setting the pressure gauge equal to 7.5 bar and is placed behind the setup at the wall.
- Valve 13 is for controlling the water flow in the cooling circuit, which must be set to avoid overflow.

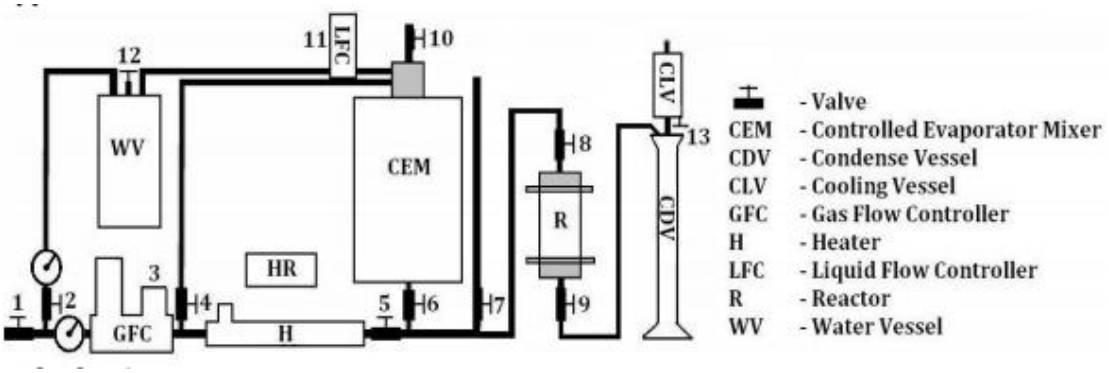

Figure G.1: A scheme of the reactor setup

For dehydration and hydration, the following steps must be followed in the same sequence.

Dehydration

System Preparation	Turn on the power supply and computer Close: 2, 4, 6, 7, 10, 11, 12, 13 Open: 1, 5, 8, 9
Start Gas Flow	Give setpoint to GFC with the Bronkhorst® software. Valve 3 opens. Determine the vapor flow at the inlet from 2.5% RH of grid air. Wait until the outlet vapor flow becomes equal to the inlet vapor flow.
Start Heater	Open: 13 Turn the heater on by using the software in the computer. Give the desired dehydration temperature and the heating rate.
Start Recording	Start recording the thermocouple and humidity measurements with the picolog recorder in the computer.
Stop the Experiment	Open: 7 Close: 8, 9 and 13 Turn off the heater Give setpoint = 0 to GFC Close: 1

Hydration

Fill the Water Vessel	Turn off the power supply Close: 1, 2, 3, 4, 5, 6, 7, 8, 9, 10, 11, and 13 Open: 12 Remove the large bolt on the top of the water vessel and fill it 2/3 of the height of the water vessel with distilled water. Close it. Close: 12 Open: 1, 4, 6, and 7 Turn on the power supply and computer. Give setpoint to GFC. Open: 2, 11, and 10. This step is not required every time. The water vessel must be checked and filled after 2-4 hydrations.
Preparing the System	Turn on the power supply and computer. Close: 3, 5, 8, 9, 10, 11, and 13 Open: 1, 4, 6 and 7
Set the CEM Heater Temperature	Give the desired setpoint in percentage in the Bronkhorst® software and wait until the temperature is reached. The CEM heater has a maximum output of 150 °C.
Start Gas Flow	Give setpoint to GFC in the Bronkhorst® software. Valve 3 opens. Wait until the outlet vapor flow becomes equal to the inlet vapor flow.
Start Liquid Flow	Open: 2 Give setpoint to LFC. Wait until stabilization.

	The maximum liquid flow that the LFC can deliver is 1000 g/h.
Start Recording	Start recording the thermocouple and humidity measurements with the picolog recorder in the computer.
Connect Reactor	Open: 8 and 9 Close: 7
Stop the Experiment	Open: 7 Close: 8 and 9 Give setpoint = 0 to LFC Close: 2 Give setpoint = 0 to GFC and CEM temperature controller Close: 1

In case of an emergency

Shut the power supply with the red button behind the table. To release reactor pressure, open valve 7 and 9 to flush the air. To prevent an overflow of water in the cooling circuit, close the water supply valve behind the table on the wall. To stop immediately the air flow, close valve 1 placed behind the table at the wall.

Bronkhorst® Software

To operate the Bronkhorst® software Start → Program → Bronkhorst → FlowDDE V4.58 When the FlowDDE V4.58 is opened Communication → Open Communication After communication, minimize the window
To give setpoints in percentage to the GFC, LFC and CEM heater Start → Program → Bronkhorst → FlowPlot V.3.21 When the FlowPlot V.3.21 is opened Instrument settings → Setpoint Controller By changing the channel at the setpoint controller the GFC, LFC or CEM channel can be selected Channel 1 → color blue → CEM Heater Controller Channel 2 → color yellow → LFC Channel 3 → color red → GFC The setpoint of the instrument is selected → Send → Change the channel → Give next setpoint for the other channel

Thermocouple and Humidity Measurements

Picolog Recorder To start recording the measurements of thermocouple Desktop → Pico Recorder Window is opened → Create a new file to save measurements → Press the play button to start recording → When the experiment is finished, press the stop button

Appendix H
Constant Values

Table H.1: Constant Values used in this project

Property	Symbol	Value	Unit
Bed Porosity after dehydration	ϵ_b	0.6	[-]
Bed Porosity after hydration	ϵ_b	0.54	[-]
Particle Density –Anhydrous K_2CO_3	ρ_p	2330	kg/m^3
Particle Density –Sesquihydrate K_2CO_3.1.5 H_2O	ρ_p	2180	kg/m^3
Particle Heat Capacity –Anhydrous K_2CO_3	C_p	852	J/(kg·K)
Particle Heat Capacity – Sesquihydrate K_2CO_3.1.5 H_2O	C_p	2486	J/(kg·K)
Bed Height	H	0.12	m
Reactor Inner Diameter	D	0.07	m
Teflon Layer Thickness	t_{tef}	0.075	m
Wall Thickness	t_{ss}	0.01	m
Insulation Thickness	t_{ins}	0.03	m
Mass of K_2CO_3 composite	$m_{K_2CO_3}$	0.423	kg
Formation enthalpy of K_2CO_3	ΔH	-63.6	kJ/mol
Formation entropy of K_2CO_3	ΔS	-155	J/(mol·K)
Inner radius	r_1	0.035	m
Teflon layer radius	r_2	0.11	m
Stainless-steel layer radius	r_3	0.12	m
Insulation layer radius	r_4	0.15	m
Reactor length	L	0.12	m
Convective heat transfer coefficient of air	h	2.39	W/(m^2·K)
Specific heat capacity of air	$C_{p_{air}}$	1000	J/(kg·K)
Viscosity of air	μ_{air}	1.85×10^5	kg/(m·s)
Thermal conductivity of air	λ_{air}	0.03	W/(m·K)
Thermal conductivity of Teflon	λ_{tef}	0.25	W/(m·K)
Thermal conductivity of stainless-steel	λ_{SS}	13.4	W/(m·K)
Thermal conductivity of glass-wool insulation	λ_{ins}	0.04	W/(m·K)
Volume of K_2CO_3 composite in the reactor	$V_{K_2CO_3}$	4.23×10^{-4}	m^3
Particle diameter of K_2CO_3 composite	d_p	2	mm
Air density	ρ_{air}	1	kg/ m^3
Air velocity	u	0.26	m/s